Chapter 3

Preparation, Characterization and Applications of Visible Light Responsive Photocatalytic Materials

Arpita Pandey[1], Sangeeta Kalal[1], Nutan Salvi[1], Chetna Ameta[1], Rakshit Ameta[2] and Pinki B. Punjabi[1*]

[1]Photochemistry Laboratory, Department of Chemistry, University College of Science, M. L. Sukhadia University, Udaipur - 313002, Rajasthan, India

[2]Department of Chemistry, J.R.N. Rajasthan Vidyapeeth University, Udaipur - 313001, Rajasthan, India

E-mail: pb_punjabi@yahoo.com

Abstract

Today, scientists all over the world are looking for eco-friendly methods to treat polluted water for its reuse. Photocatalytic activity (PCA) depends on the ability of the catalyst to create electron–hole pairs, which generate free radicals (e.g. hydroxyl radicals: $^{\bullet}OH$), which undergo in secondary reactions as efficient oxidant under irradiation of light. Various applications of visible light active (VLA) photocatalytic materials, in terms of environmental remediation are- Elimination of several pollutants (e.g. alkanes, alkenes, phenols, pesticides, etc.) particularly in water treatment, disinfection and air purification, self-cleaning glass, photocatalytic concrete and paints; photoreduction of carbon dioxide; outdoor and indoor coatings of photocatalysts for roads and buildings. Therefore, the main objective of this proposal is to review the eco-friendly heterogeneous catalytic systems with low cost starting compounds with the benefit that no sludge formation is there and catalysts are reusable too.

Keywords

Photocatalyst, Semiconductor, Band Gap, Photocatalytic Degradation, Water Pollution, Advanced Oxidative Processes, Binary, Ternary and Quaternary Photocatalyst

Contents

1. Introduction

Environment is the surrounding which includes living things and natural forces. The environment of living things provides the conditions for development and growth, as well as it also causes danger and damage, if not cared for. Pollution is the introduction of contaminants into the environment that causes adverse changes. Water pollution is due to the presence of non-biodegradable dyes along with some other toxic pollutants like metals, acid, alkali, carcinogenic aromatic amines, etc. in the industrial effluents. Water pollution due to effluents coming from textile dyeing industry is a cause of serious concern. The techniques for detection of dyes are cost intensive and futile because the dyes undergo chemical changes under environmental conditions and the transformation products may be more toxic and carcinogenic than the parent molecule.

Dye wastes represent one of the most problematic groups of pollutants because they can be easily identified by the human eye and are not easily biodegradable. Dyes may be of a number of structural varieties like acidic, basic, disperse, azo, anthraquinone based and metal complex dyes. Weber and Adams [1] studied that during the coloration process; a large percentage of the synthetic dye does not bind and is lost to the waste stream. Approximately 10-15% dyes are released into the environment during dyeing process making the effluent, highly colored and aesthetically unpleasant. Wang et al. [2] reported that the effluent coming from textile industries carries a large number of dyes and other additives, which are added during the coloring processes. These are difficult to remove in conventional water treatment procedures and can be transported easily through sewers and rivers especially because they are designed to have high water solubility.

The detection of dyes is a difficult process because of the large variety of functional groups in different dyes and their diverse properties. Analytical procedures, which are used for determination of dyes at parts per million (ppm) levels, are very limited. Most of the dyes are non-volatile; and hence, gas chromatography cannot be used. Tincher and Robertson [3] studied the use of high pressure liquid chromatography (HPLC) and mass spectrometry for analysis of some of the dyes. Various processes, which are used for the treatment of dye waste, include biological treatment, catalytic oxidation, filtration, and sorption process and combination treatments. The textile industry is one of the largest polluters in the world. The World Bank estimates that almost 20% of global industrial water pollution comes from the dyeing of textiles.

A large amount of fresh water is being used for dyeing, rinsing, and treatment of textiles. A single T-shirt made from conventional cotton requires 2700 liters of water, and a third of a pound of chemicals. Millions of gallons of wastewater are discharged each year by mills and industries, which contain chemicals such as formaldehyde (HCHO), chlorine and heavy metals such as lead and mercury. These chemicals cause both environmental damage and cause human disease.

1.1 Textile manufacturing dyes release

- Aromatic amines (benzidine and toluidine), heavy metals, ammonia, alkali salts, toxic solids and large amounts of pigments
- Chlorine, a known carcinogen

Untreated dyes cause chemical and biological changes in our aquatic system, which threaten life of many fishes and aquatic plants. The enormous amount of water which is required by textile production competes with the growing daily water requirements of the half billion people that live in drought-prone regions of the world. By 2025, the number of inhabitants of drought-prone areas is projected to increase to almost one-third of the world's population. If global consumption of fresh water continues to double every 20 years, the polluted waters resulting from textile production will pose a great threat to human lives.

Phenols, also known as total phenols or phenolics, are important due to their widespread use in many manufacturing processes. Phenols pose a serious threat to many ecosystems, water supplies and human health because of their inertness, toxicity, endocrine disrupting abilities and carcinogenic behavior [4, 5]. The United States, Canada and the European Union have included some phenols in their list of priority pollutants [6–8]. Phenol is commonly employed in the manufacturing of phenolic resins, bisphenol A, caprolactam and chlorophenols such as pentachlorophenol [4]. Cresols are isomeric mono-substituted phenols. Commercially, cresol is produced as a by-product from the fractional distillation of crude oil and coal tars and the gasification of coal. Phenol and its derivatives have been identified as effluents coming from petroleum refining [9], pulp and paper manufacturing [10], coal processing [11] and chemical production facilities [12]. Oil-shale processing is another industry that produces effluents containing phenol and cresols [13]. Removing phenolic compounds from wastewaters and drinking water supplies has received widespread attention recently because of their toxic and endocrine disrupting properties [14]. Phenols can be removed by physical processes such as flocculation, precipitation, granular activated carbon (GAC) or reverse osmosis (RO) [15].

The presence of dyes or their degradation products in water even at very low concentration can cause human health disorders like nausea, haemorrhage, ulceration of skin and mucous membranes and can cause severe damage to kidneys, reproductive system, liver, brain and central nervous system. Hence, it is essential to devise some methods to successfully remove them.

Photocatalysis is a surface phenomenon initiated by the irradiation of UV/ visible light of higher energy than the band gap of the photocatalyst used. The surface properties involving the nature of active sites and its number play a key role in determining the photocatalytic reactivity of the catalysts. Photocatalysis has been regarded as a green, simple, and low-cost method to degrade dyes.

Gogate and Pandit [16] reviewed advanced oxidative processes (AOP), these are successful in removing complex organic contaminants because they can achieve complete oxidation. AOP offer a distinct advantage over many conventional treatment methods, such as biological processes, because faster degradation rates are accomplished and contaminants are degraded completely rather than being transferred from one phase to another. Wang et al. [17] observed that in advanced oxidative processes (AOP), there is no requirement for by-product disposal. Matilainena and Sillanpaa [18] studied that AOP processes can be configured using a combination of chemical and physical agents such as a combination of oxidizing agents, an oxidizing agent plus ultraviolet, catalyst or ultrasound and a catalyst plus ultraviolet. Glaze et al. [19] reported that the degradation of organics is mediated by the generation of •OH radicals in all AOP processes.

1.2 Visible light photoactive materials

Light is the electromagnetic radiation within a certain portion of the electromagnetic spectrum. The word usually refers to "visible light", which is visible to the human eye and is responsible for the sense of sight. Visible light is usually defined as having a wavelength in the range of 400 to 700 nm; between the infrared (with longer wavelengths) and the ultraviolet (with shorter wavelengths). The main source of light on Earth is the Sun. Heterogeneous photocatalytic technologies have been applied to control the organic pollutants and microorganisms in water. Development of narrow band-gap photocatalysts which function in the visible light remains a challenge in the wastewater treatment processes.

1.3 Binary photocatalysts

Binary photocatalysts are those catalysts, which are composed of two catalysts, which are active in the presence of light. Binary mixed TiO_2:SiO_2 was reported to have higher photocatalytic activity than a titania only. Jung and Park [20] reported that addition of

silica into titania enhances the thermal stability as well as increases the specific surface area and acidity. Guillard et al. [21] have observed that the process of preparation for TiO_2:SiO_2 films can avoid the filtration problems of the slurry. Oh et al. [22] studied the photo-oxidative transparent TiO_2:SiO_2 films on glass which form the basis for self-cleaning indoor windows, lamps, and automotive windshields.

Do et al. [23] and Papa et al. [24] found that the degradation rates of 1, 4-dichlorobenzene was increased by a factor of 3 by calibrating 3 mole % addition of WO_3 and MoO_3 in titania. They found a strong correlation between surface acidity and reactivity. Surface acidity is thought to take the form of stronger surface hydroxyl groups. These hydroxyl groups accept the holes generated by illumination and as a result, oxidize adsorbed molecules. Hole traps such as the hydroxyl groups prevent the electron-hole recombination and therefore, increases quantum yield. Thus, the greater number of surface hydroxyl groups yields the higher reaction rate [25].

TiO_2–Al_2O_3 binary oxide surfaces were utilized in order to develop an alternative photocatalytic NO_x abatement approach, where TiO_2 sites were used for ambient photocatalytic oxidation of NO with O_2 and alumina sites were exploited for NO_x storage. To perform complete photocatalytic reduction of NO_x, an alternative NO_x abatement strategy has been demonstrated, which includes photocatalytic oxidation of NO_x on a TiO_2/Al_2O_3 binary oxide photocatalyst surface and its storage in the solid state in the form of nitrates and nitrites. This alternative strategy was inspired by some studies on NSR technology (NO_x storage and reduction), which is used for the thermal catalytic after treatment of automotive NO_x emissions [26-28].

Individual CdS photocatalyst has very low separation efficiency of photogenerated electron-hole pairs and undergoes photocorrosion, which limits its practical application [29]. In order to improve its photoactivity and to inhibit the photocorrosion, cadmium sulfide is usually coupled with other semiconductors, including CdS/TiO_2 [30–32], CdS/ZnO [33, 34], CdS/ZnS [35], CdS/WO_3 [36] as well as CdS/MoS_2 [37]. The rate of hydrogen evolution on MoS_2/CdS was higher than on CdS particles loaded with other metal catalysts such as Pt, Ru, Rh, Pd and Au. This result was explained by the better electron transfer between MoS_2 and CdS [37].

A novel Ti(IV) / Fe(III) mixed oxide catalyst has shown an increased photocatalytic activity for destruction of dichloroacetic acid at 450 nm [38]. The photocatalytic activity of iron doped TiO_2 or mixed oxide of different proportions of Fe and Ti, prepared by impregnation and coprecipitation methods has been shown to be active in the visible light for the photoreduction of N_2 [39], degradation of oligocarboxylic acid [40], 4-nitrophenol [41] and $CHCl_3$ oxidation [42] etc. Activity of these catalysts was higher than that of pure

hydrous oxide prepared under similar conditions. Navio et al. [43] have prepared the specimen with higher Fe (III) content and showed its photoactivity in the visible light. It has also been found that the catalytic activity of Fe/Ti mixed oxides largely depends on preparation methods, iron content, sintering temperature and phase composition.

The measurement of photoluminescence of the photocatalysts is one of the most important and useful ways to elucidate the surface properties related to adsorption, catalysis, and photocatalysis and reactivity of photocatalyst [44]. The photoluminescence spectrum of TiO_2 nanoparticles is efficiently quenched by the addition of oxygen onto the surface through an increase in the extent of the band bending of TiO_2 photocatalyst due to the adsorption of O_2^- species [45, 46]. The relative reactivity of photocatalysts toward oxygen molecule was estimated by the quenching degree of the photoluminescence by the addition of O_2. The intensity of the photoluminescence was decreased to 89% of its original intensity for SiO_2/TiO_2, 37% for TiO_2 and 26% for boron-SiO_2/TiO_2, respectively in the presence of 20 Torr of O_2 [47].

Yang and Swisher [48] reported that the photocatalytic efficiency of the photocatalysts can be enhanced by coupling ZnO with TiO_2. Wang et al. [49] reported that binary oxides can provide a more efficient charge separation, increased lifetime of charge carriers and enhanced interfacial charge transfer to absorbed substrates. Liao et al. [50] studied the preparation and photocatalytic activity of the binary oxide photocatalyst ZnO/TiO_2 in the degradation of methyl orange dye. It was shown that the addition of ZnO enhanced the photocatalytic activity of TiO_2 significantly.

1.4 Ternary photocatalysts

Graphene is proposed to serve as an efficient acceptor for the photogenerated electrons in graphene–TiO_2 nanocomposites and thus, significantly suppresses the charge recombination and enhancing the photocatalytic rate of the nanocomposite as compared to that of pure TiO_2 nanoparticles (NPs) [51,52]. Lin et al. [53] reported that a ternary nanocomposite of graphene–TiO_2– Fe_3O_4 (GTF) possesses the integrated functions as well as a low-cost, recollectable and stable photocatalyst for the degradation of organic dyes namely rhodamine B (Rh B), methyl orange and acid blue 92.

Bi_2WO_6 possess interesting physical properties such as ferroelectric piezoelectricity, pyroelectricity, catalytic behavior, and a non-linear dielectric susceptibility [54,55]. Bi_2WO_6 show a great potential as a visible-light-active photocatalyst for organic compound degradation and O_2 evolution under visible light irradiation [56, 57]. Tang et al. [58] reported that Bi_2WO_6 showed the activity of mineralizing both; $CHCl_3$ and CH_3CHO contaminants under visible light irradiation.

The sphere-like bismuth tungstate (Bi_2WO_6) was synthesized with silica protection calcination by using a facile hydrothermal method. The flower-like bismuth tungstate (Bi_2WO_6) was also synthesized without silica protection. Natrajan et al. [59] reported the use of sphere and flower-like Bi_2WO_6 for the degradation of reactive black 5 (RB 5) in the presence of visible light. The bandgap of mesoporous nanocrystalline TiO_2 was modified with Li, Mg, Pd and Sr, metal ion salt solution using wet impregnation. Ion impregnated samples were used as photocatalysts for the degradation of organic contaminants [60]. Pathak et al. [61] reported that the nanocrystals of Mg-Mn ferrites were used for the degradation of nitrobenzene.

Ternary chalcogenide nanocrystals such as $Cd_{1-x}Zn_xS$ [62], $Cd_{1-x}Zn_xSe$ [63], and $CdS_{1-x}Se_x$ [64] have received considerable attention because their composition-tunable band edge offers new opportunities to harvest light energy in the entire visible region of solar spectrum. A ternary chalcogenide nanocrystal shows various potential applications in a wide array of fields, which include photovoltaics [65], photocatalysis [66], and photoelectrochemical cells [67]. When photons are completely absorbed, photon energy that exceeds semiconductor band gap is dissipated as heat due to the vibrational relaxation of excitons [68]. Because of the heat loss, a substantial amount of solar energy has already been consumed, before it can be converted into other accessible energies. This obstacle needs to be circumvented to promote the advancement of photocatalysis technology for solar fuel production.

Aguiar et al. [69] reported that the rare earth oxides are broadly used in luminous materials, polishing powder, electronic ceramics, and efficient catalyst in photocatalytic field. Heteropoly compounds like $H_3PW_{12}O_{40}/TiO_2$ [70], $NdPW_{12}O_{40}/TiO_2$ [71], $BiPW_{12}O_{40}$ [72], $Cu_3(PW_{12}O_{40})_2$ [73] had high photocatalytic activities in photocatalytic elimination of formaldehyde, acetone, and methanol.

Wide band gap p-block metal semiconductors like Ga_2O_3, In $(OH)_3$, InOOH and $Sr_2Sb_2O_7$ [74] show high activity and stability in the photocatalytic degradation of benzene. The high photocatalytic performance observed over these wide band gap p-block metal semiconductors is related to their peculiar electronic structure.

Wide band gap endows the photogenerated charge carriers in these semiconductors with redox ability strong enough to react with surface adsorbed H_2O to produce $^{\bullet}OH$ radicals. In this way, the degradation of benzene can proceed via the $^{\bullet}OH$ radical pathway, which makes these wide band gap p-block semiconductors capable of maintaining a clean catalyst surface and a long stability during the photocatalytic reaction studies. The wide band gap p-block metal semiconductors are a new generation of photocatalysts for benzene degradation. Besides this, except the common characteristics like wide band gap

and the dispersive conduction band, other factors influencing their photocatalytic activity for benzene degradation remain largely unclear. For this purpose, more wide-band gap p-block metal semiconductors should be investigated especially ternary ones due to their diversified crystallographic and electronic structure and their photocatalytic activity.

Ag_3PO_4 also has a quantum efficiency of 90% at wavelengths longer than 420 nm [75] and shows high photocatalytic activity owing to its absorption in the visible portion of the solar spectrum and high charge carrier mobility because of the delocalized charge distribution of the conduction-band minimum, which results in a small electron effective mass, beneficial for the surface carrier mobility [76]. Graphitic carbon nitride (g-C_3N_4) is based on the stacked two-dimensional structure analogous of graphite with N replacing non-adjacent carbon atoms. Wang et al. [77] used graphitic carbon nitride (g-C_3N_4) in water splitting application as a metal-free photocatalyst operating under visible light irradiation. Various g-C_3N_4 based hybrid photocatalysts including g-C_3N_4/$BiPO_4$ [78], graphene/g-C_3N_4 [79], g-C_3N_4/ Bi_2WO_6 [80], Fe-g-C_3N_4-LUS-1 [81], g-C_3N_4/SiO_2-HNb_3O_8 [82], and g-C_3N_4/TaON [83] have been developed to further extend the visible light absorption range and the photogenerated carriers separation efficiency. Shen et al. [84] reported that Ag/Ag_3PO_4/g-C_3N_4 hybrid system exhibits superior photocatalytic performance for rhodamine B degradation compared with a binary Ag_3PO_4/g-C_3N_4 photocatalyst, or Ag_3PO_4 and g-C_3N_4 as individual components. It was found that this photodegradation strongly depends on the proportion of silver nanoparticles on the Ag_3PO_4 surface and the ratio of the components in the Ag_3PO_4/g-C_3N_4 hybrid. The enhanced photoactivity can be attributed to the surface plasmon resonance (SPR) originating from silver nanoparticles and the heterojunction-like interface between Ag_3PO_4 and g-C_3N_4.

Kim et al. [85] reported the synthesis of CdS/TiO_2/WO_3 ternary hybrid systems as new photoactive composites and found that the ternary hybrid exhibited much higher photocatalytic activity than that of CdS alone or binary hybrids. Lin et al. [86] prepared CdS nanoparticles/ZnO shell/TiO_2 nanotube (NT) arrays for water splitting and observed that the conversion efficiency increased from 0.39% to 1.30%. Chen et al. [87] described a new method to form a ZnO energy barrier layer between TiO_2 NTs and CdS quantum dots, which exhibited improved efficiency of the quantum dots-sensitized solar cells.

1.5 Quaternary photocatalysts

Quaternary thin films were reported for use as the photoabsorber in solar cells because of direct band gap and high optical absorption coefficient. Cu_2ZnSnS_4 (CZTS) thin films are used as the photoabsorber in photovoltaic cells because of its low cost, non-toxic constituents, direct band gap and high optical absorption coefficient as high as 104 cm^{-1}.

Bwamba et al. [88] reported the optical absorption studies of the annealed CZTS films. The absorption spectra indicated that annealed films have a high absorbance of light in the visible region. Yeh and Cheng [89] reported the preparation of the Ag-Zn-Sn-S quaternary thin films using chemical bath deposition technique. The X-ray diffraction patterns of the samples reveal that tetragonal Ag_2ZnSnS_4 phase, with small amount of impurities such as Ag_8SnS_6 and SnS can be obtained using TEA as the chelating agent and deposition temperature 70 °C.

Quaternary metal oxide photocatalysts such as $Ni_xIn_{1-x}TaO_4$ [90], $K_3Ta_3Si_2O_{13}$ [91], and $Sm_2Ti_2O_5S_2$ [92] display enhanced photocatalytic activity in contrast to the conventional photocatalysts viz. $TiO_{2-x}N_x$ [93], TaON [94] and $(Ga_{1-x}Zn_x)$ $(N_{1-x}O_x)$ [95] because such crystal lattice possess large population of catalytically active sites [92]. Because of its low band gap, Pb_2FeNbO_6 (PFNO) is used in ferroelectrics, sensors, photocatalysis, photoelectrochemical hydrogen production [96].

$PbBiO_2Br$ (anisotropic 2D structure) has been used as a photocatalyst due to a band gap of 2.47 eV and its unique layered structure [97]. In anisotropic 2D structure, photoinitiated charge carriers experience two kinds of the confinement. The strong confinement (thickness) is necessary to increase sufficiently the free energy of conduction band electrons for photocatalytic reaction; meanwhile, the weak confinement (length and width) [98] is needed to facilitate effective delocalization of longer-living excitons and separated charges [99]. Therefore, the probability of photoinduced electron-hole recombination is effectively minimized.

Nb-containing oxides such as $CsBiNb_2O_7$, $CsBi_2Nb_5O_{16}$, and $PbBi_2Nb_2O_9$ were used for the decomposition of gaseous 2-propanol in the presence of visible light. The photocatalytic activity of $CsBi_2Nb_5O_{16}$ was higher than that of $CsBiNb_2O_7$ [100] and $PbBi_2Nb_2O_9$ (Eg = 2.88 eV) was much more active than $TiO_{2-x}N_x$ (Eg = 2.73 eV) [101]. $RbBi_2Nb_5O_{16}$ and $RbBiNb_2O_7$ decomposed gaseous acetaldehyde and $RbBi_2Nb_5O_{16}$ showed a higher photoactivity than $RbBiNb_2O_7$ in accordance with their different absorption properties [102]. $LiBi_4M_3O_{14}$ (M = Nb, Ta) was used for the degradation of various dyes and phenolic compounds under UV irradiation [103]. $LiBi_4Nb_3O_{14}$ was more efficient for the degradation of the phenolic compounds, due to its lower band gap (3.0 eV) and preferential affinity of niobium for the phenolic functional groups. Bi_2InTaO_7 obtained by the sol–gel method showed a high efficiency for the UV-induced degradation of alizarin red S [104]. Li et al. [105] synthesized polycrystalline Ag_2ZnGeO_4 at 220 ^oC by the cation exchange method with Na_2ZnGeO_4 as the parent compound. The Ag_2ZnGeO_4 sample showed good activity for the photodegradation of rhodamine B and orange II. $PbBiO_2Br$, tested for the degradation of methylene blue and

methyl orange, and it was found more photocatalytically more active than $PbBi_2Nb_2O_9$, $TiO_{2-x}N_x$ and BiOBr under visible light [106].

2. Preparation and characterization of various photocatalysts:

2.1 Binary photocatalysts

2.1.1 Preparation of TiO_2:SiO_2 thin films

Solutions of $(NH_4)_2TiF_6$ (0.1 mol·L^{-1}) and $(NH_4)_2SiF_6$ with a Si/Ti atomic ratio of 15% in treated solutions were mixed as a parent solutions for the liquid phase deposition (LPD) process [107]. Very small amounts of nanocrystalline TiO_2 and amorphous SiO_2 seeds were dissolved in the mixed solutions. The solutions were stirred for 24 h and then filtered. After the introduction of H_3BO_3 having a concentration of 0.3 mol·L^{-1} into the precursor solutions, the chemical reactions cause the formation of TiO_2 and SiO_2 precipitates. The slide-glass substrates were ultrasonically cleaned with diluted nitric acid, ethanol, and distilled water. These were then immersed vertically into solutions of the reactive precursor for 9 h. During the deposition, the precursor solutions were kept at a constant temperature of 35 ^oC. The TiO_2 and the SiO_2 precipitates in the solutions were deposited on glass substrates. The deposited films were washed in distilled water, dried naturally at ambient temperature, and annealed at temperatures ranging from 100 to 500 ^oC in intervals of 100 ^oC for 1 h in air.

From SEM of annealed TiO_2:SiO_2 thin films, it was concluded that many interspaces among the particles and nanopores on the top of TiO_2 particles are present at low temperatures due to the stress at the interface between TiO_2 and SiO_2. Higher was the annealing temperature, the larger is the particle size, and the fewer will be the interspaces and nanopores. The specific surface areas of the samples gradually decrease with increasing annealing temperature due to the formation of larger clusters and to the disappearance of nanopores as a result of stress release after annealing. A decrease in the surface area means a declined number of active sites, where the holes are bound with hydroxyls and participate in the redox reaction, which implies a decrease in the photocatalytic activity [108].

In FTIR spectra of binary TiO_2:SiO_2 thin films, a band was observed at 3700 cm^{-1} due to the stretching vibration of hydroxyl groups, but the Ti-OH stretching vibration bands become much weaker when the annealing temperature was higher than 100 ^oC, which means that a certain number of OH groups is progressively removed during the annealing. The disappearance of the Ti-OH vibration modes after annealing at temperature above 300 ^{0} C indicates directly an elimination of hydroxyl groups.

2.1.2 Preparation of TiO_2/Al_2O_3 binary oxides

Titanium (IV) isopropoxide (TIP) and aluminum-tri-sec-butoxide (ASB) were used as the main ingredients in the preparation of the TiO_2/Al_2O_3 binary oxides via sol–gel method [109-111]. The samples are labeled as "xTi/Al-y", where x represents the TiO_2 to Al_2O_3 mole ratio (i.e. 0.25, 0.5 and 1.0) and y represents the calcination temperature (150–1000 oC) of the sample. Depending on the corresponding TiO_2–Al_2O_3 mole ratio, an appropriate amount of ASB was mixed with propan-2-ol and acetylacetone for 30 min during the synthesis of TiO_2/Al_2O_3 binary oxide. TIP was added in a drop wise fashion to the mixture over the course of another 30 min. All of the synthesis steps were carried out at room temperature under vigorous stirring. The co-precipitation of the obtained hydroxides was accomplished after the gradual addition of 0.5 M HNO_3 (aq) to the solution, which leads to the formation of a gel. The resulting yellow gel was aged under ambient conditions for 2 days and the dried sample was ground to form a fine powder. Now, synthesized TiO2/Al2O3 binary oxides were calcined in air for 2 h at various temperatures ranging from 150 to 1000◦C.

2.1.3 Characterization of TiO_2/Al_2O_3 binary oxides

Diffuse reflectance UV–VIS (DR-UV–VIS) spectra were utilized in order to obtain electronic band gap values (Fig. 1). Fig. 1 indicates that for the 1.0 Ti/Al photocatalyst family, no significant photocatalytic activity was detected up to 800°C, while at this calcination temperature, a remarkable increase in the activity was observed, though this catalyst is not as effective as the 05 Ti/Al-900 catalyst in total NO_x abatement, due to the significant the significant NO_2 (g) generation of the former. It was observed that for calcination temperatures above 800 °C, NO_x abatement starts to fall, as evident by the increased NO_2 (g) slip into the atmosphere as well as decreasing NO_x storage in the solid state. 0.5 Ti/Al-900 binary oxide catalyst shows the highest NO_x abatement performance among all of the analyzed photocatalysts, where it performs 160% higher NO_x storage and 55% lower NO_2 (g) release to the atmosphere compared to the Degussa P25.

All of the NO_x adsorption/storage (i.e. Al_2O_3) sites cannot be utilized at low TiO_2 loadings, due to limited photo-oxidation capability of the inadequate number of TiO_2 oxidation sites on the surface. At very high TiO_2 loadings, TiO_2 covers most of the Al_2O_3 surface and upon calcination above 800 °C, SSA of the catalyst sample falls drastically together with the formation of crystalline anatase and rutile mixture; limiting the available number of NO_x storage sites that are available after photooxidation. Onset of photocatalytic activity was observed in a rather sharp manner at 950, 900 and 800 °C for the 0.25 Ti/Al, 0.5 Ti/Al and 1.0 Ti/Al samples, respectively. As the relative TiO_2 loading

in the TiO_2/Al_2O_3 binary oxide samples increases, onset temperature for the photocatalytic activity shifts to lower temperatures.

Electronic band gap values for the relatively inactive amorphous Ti/Al samples reveal a characteristically high value within 3.4–3.6 eV, which are calcined at lower temperatures. With the onset of the photocatalytic activity, a very sharp fall in the electronic band gap values were observed, where the band gap decreases to a typical value of 3.05–3.10 eV, in line with the formation of ordered anatase and rutile phases. Typical band gap values for bulk anatase and rutile phases are ca 3.2 and 3.0 eV, respectively [112]. Thus, for the active photocatalyst samples, the band gap value is in between that of anatase and rutile, being closer to the latter, in accordance with the fact that in the most active photocatalyst, rutile exists as the predominant phase together with anatase as the minority phase. Electronic band gap cannot be used as a sole indicator for the estimation of the photocatalytic activity trends due to the fact that once the photocatalytically active structure is obtained leading to a drastic decrease in the electronic band gap. Band gap values cease to change at higher calcination temperatures although photocatalytic activity starts to decline.

2.1.4 Preparation of binary CdS-MoS_2 composites

A typical hydro/solvothermal mixed solution process was used for the preparation of CdS-MoS_2 composites with various molar ratios of semiconductors [113]. The prepared mixture was placed in the autoclave and heated at 200℃ for 24 h. The resulting precipitate was washed with distilled water and ethanol, respectively and dried in the oven at 70℃ for 8 h.

2.1.5 Characterization of binary CdS-MoS_2 composites

SEM images of binary CdS-MoS_2 composites with different CdS and MoS_2 molar ratios are shown in Fig. 1. In the case of CdS-MoS_2 5-1 sample containing the highest molar ratio of CdS, nanoleaf structure indicating the presence of CdS was observed. The increase of MoS_2 ratio resulted in the formation of hexagonal shaped nanostructures with average edge size of about 100–125 nm (Fig. 1b). Further increase in molar ratio of MoS_2 to CdS causes a large change in microstructures (Fig. 1c and 1d). Bonded structures of microspheres with diameters ranging from 0.08 to 1 μm were observed.

Fig. 2 depicts the spectra for pure CdS and MoS_2 semiconductors and their binary composites with varying molar ratio between CdS and MoS_2. The absorption edge of single CdS is about 510 nm, which coincides with the literature. It was previously reported that the absorption properties of CdS are strongly shape-dependent [114]. Liu et al. [115] reported enhanced absorption properties for CdS-MoS_2 composites for

photocatalytic H_2 production. As compared with single CdS, composites with excess of CdS exhibited a red shift and a less steep absorption edge as well as absorption was more intense for composites containing excess MoS_2.

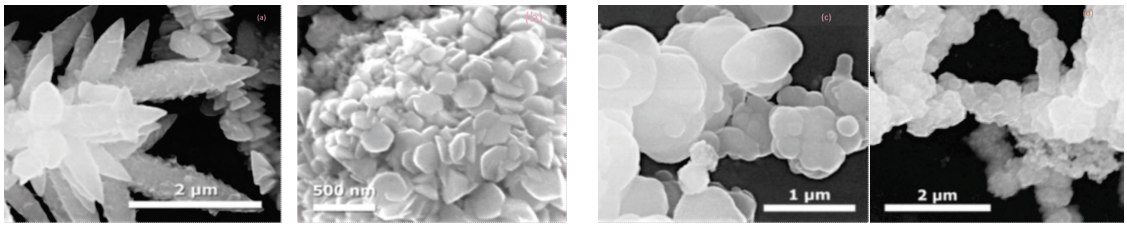

(a) (b) (c) (d)

Figure 1. SEM images of binary CdS-MoS_2 composites obtained by solvothermal mixed solution methods with different molar ratio of CdS: (a) CdS:MoS_2 = 5:1; (sample CdS-MoS_2 5-1); (b) CdS:MoS_2 = 4:1 (sample CdS-MoS_2 4-1); (c) CdS:MoS_2 = 1:1 (sample CdS-MoS_2 1-1); and (d) CdS:MoS_2 = 1:5 (sample CdS-MoS_2 1-5). (Reproduced with permission from Beata Bajorowicz, Anna Cybula, Michał J. Winiarski, Tomasz Klimczuk and Adriana Zaleska, Surface properties and photocatalytic activity of $KTaO_3$, CdS, MoS_2 semiconductors and their binary and ternary semiconductor composites, Molecules 2014, 19, 15339-15360).

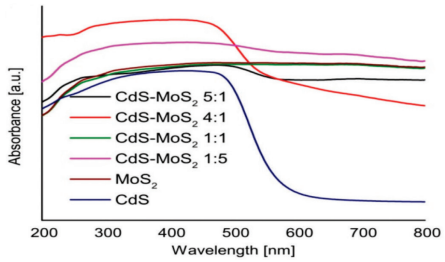

Figure 2. The UV-Vis diffuse reflectance spectra of single CdS, MoS_2, and binary CdS-MoS_2 nanocomposites. (Reproduced with permission from Beata Bajorowicz, Anna Cybula, Michał J. Winiarski, Tomasz Klimczuk and Adriana Zaleska, Surface properties and photocatalytic activity of $KTaO_3$, CdS, MoS_2 semiconductors and their binary and ternary semiconductor composites, Molecules 2014, 19, 15339-15360).

2.2 Ternary photocatalysts

2.2.1 Preparation of $KTaO_3$-CdS-MoS_2 composites

A typical hydro/solvothermal mixed solutions process was also used for the preparation of $KTaO_3$-CdS-MoS_2 composites with various molar ratios of semiconductors [113]. The prepared mixture was placed in the autoclave and heated at 200℃ for 24 h. The resulting

precipitate was washed with distilled water and ethanol, respectively and dried in the oven at 70℃ for 8 h.

2.2.2 Characterization of $KTaO_3$-CdS-MoS_2 composites

SEM of $KTaO_3$-CdS-MoS_2 composites are given in Fig. 3. The transition of the $KTaO_3$ structure from cubic to octahedral was observed for the samples $KTaO_3$-CdS-MoS_2 10-1-1 obtained by solvothermal mixed solutions. Solvothermal mix solutions method did not cause dramatic changes in the structure cubes nor was nano leaf observed (Fig. 3c). In calcinated $KTaO_3$-CdS-MoS_2 10-5-1 composite, nano leaves of CdS was deposited on the surface of large cubes of $KTaO_3$ (Fig. 3d).

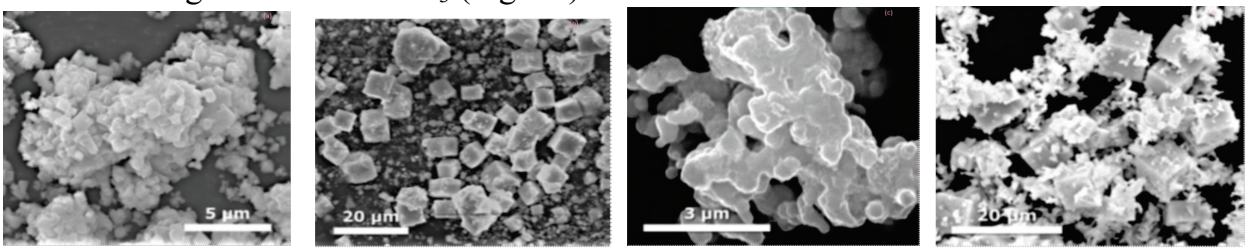

(a) (b) (c) (d)

Figure 3. SEM images of ternary $KTaO_3$-CdS-MoS_2 composites obtained with different molar ratio and using two different preparation route: (a) $KTaO_3$-CdS-MoS_2 (10:1:1) obtained by solvo thermal mixed solutions (sample $KTaO_3$-CdS-MoS_2 10-1-1_MS); (b) $KTaO_3$-CdS-MoS_2 (10:1:1) obtained by calcination of single previously synthesized semiconductors (sample $KTaO_3$-CdS-MoS_2 10-1-1_C); (c) $KTaO_3$-CdS-MoS_2 (10:5:1) obtained by solvo thermal mixed solutions (sample $KTaO_3$-CdS-MoS_2 10-5-1_MS); and (d) $KTaO_3$-CdS-MoS_2 (10:5:1) obtained by calcination of single previously synthesized semiconductors (sample $KTaO_3$-CdS-MoS_2 10-5-1_C). (Reproduced with permission from Beata Bajorowicz, Anna Cybula, Michał J. Winiarski, Tomasz Klimczuk and Adriana Zaleska, Surface properties and photocatalytic activity of $KTaO_3$, CdS, MoS_2 semiconductors and their binary and ternary semiconductor composites, Molecules 2014, 19, 15339-15360).

Fig. 4 shows the spectra for ternary $KTaO_3$-CdS-MoS_2 composites containing different amount of CdS prepared by various methods. A steep absorption edge (at about 510 nm) was observed only for a calcined composite. The best adsorption properties could probably be achieved for the ternary $KTaO_3$-CdS-MoS_2 composites containing appropriate molar ratio between semiconductors.

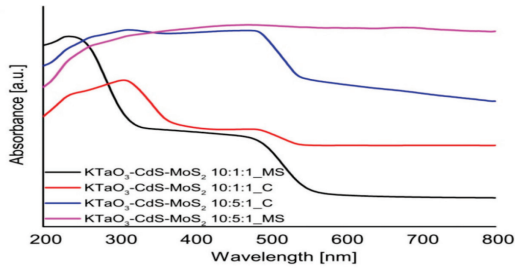

Figure 4. The UV-VIS diffuse reflectance spectra of ternary $KTaO_3$-based nanocomposites. (Reproduced with permission from Beata Bajorowicz, Anna Cybula, Michał J. Winiarski, Tomasz Klimczuk and Adriana Zaleska, Surface properties and photocatalytic activity of $KTaO_3$, CdS, MoS_2 semiconductors and their binary and ternary semiconductor composites, Molecules 2014, 19, 15339-15360).

2.2.3 Graphene–TiO_2–Fe_3O_4 (GTF)

A ternary, hybrid graphene–semiconductor–magnetic nanocomposite (graphene–TiO_2–Fe_3O_4; GTF), possesses the integrated functions [116] as:

(i) TiO_2 nanoparticles (NPs) act as a semiconductor photocatalyst to degrade the dye,

(ii) Graphene provides an effective electron pathway to suppress the charge recombination in TiO_2 and enhance its photocatalytic activity, and

(iii) Fe_3O_4 nanoparticles (NPs) act as a magnetic material for magnetic separation.

2.2.4 Preparation of graphene–TiO_2–Fe_3O_4 (GTF)

For the synthesis of GTF, graphene–TiO_2 (43 mg) was suspended in deionized water (30 mL) in a round-bottomed flask under N_2. An aqueous solution (1.56 mL) containing $FeCl_3 \cdot 6H_2O$ (3.95 mg) and $FeCl_2 \cdot 4H_2O$ (60 mg) was then injected into the flask using a pipette [117]. After stirring for 5 h under N_2, the flask was sealed after adding NH_4OH aqueous solution (4.5 mL, 1.5 m). The reaction was allowed to continue at 65 °C for 2.5 h. The product was collected by centrifugation and washed three times with water to remove excess ions before characterization. The amount of graphene–TiO_2 precursor employed was kept the same and the amounts of $FeCl_3 \cdot 6H_2O$ and $FeCl_2 \cdot 4H_2O$ were varied to obtain GTF with different ratios of Fe_3O_4 to TiO_2.

2.2.5 Characterization of graphene–TiO_2–Fe_3O_4 (GTF)

In as-obtained GTF nanocomposite, Fe_3O_4 and TiO_2 NPs can be easily distinguished by TEM image based on the differences in their size and contrast. The average size of TiO_2 and Fe_3O_4 NPs was estimated to be ca. 20 and ca. 80 nm, respectively. The powder XRD

pattern of the GTF confirmed the cubic magnetite crystal structure for Fe_3O_4 and the anatase phase with tetragonal crystal structure for TiO_2.

2.2.6 Preparation of Bi_2WO_6 nanoplates

Bi_2WO_6 nanoplates were synthesized through a hydrothermal process. The starting mixture was allowed to react in a teflon-lined autoclave at different temperatures to obtain well-crystallized nanoplates. Crystal diffraction peaks were found when the temperature was not less than 120 oC. This photocatalyst belongs to the orthorhombic system, space group Pca21. The Bi2WO6 crystal with a layered structure includes the corner-shared WO6. Bi atom layers are sandwiched between WO6 octahedral layers [118,119].

2.2.7 Characterization of Bi_2WO_6 nanoplates

Zhang et al. [120] prepared flower-like Bi2WO6 spherical superstructures by employing the similar hydrothermal method, but with an acidic (pH = 1) precursor. The flower-like microstructures were found to be constructed from nanoplates with single crystal structure. The formation of this flower-like structure was proposed to follow a three-step process: self-aggregation, Ostwald ripening and self-organization (Fig. 5).

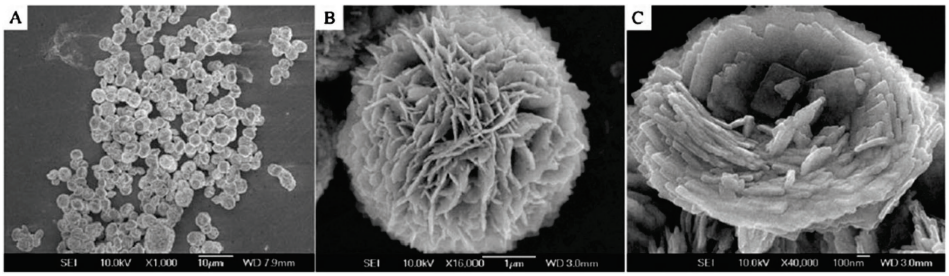

Figure 5. SEM images of flower-like Bi_2WO_6 superstructures [120]. (Reproduced with permission from Liwu Zhang and Yongfa Zhu, A review of controllable synthesis and enhancement of performances of bismuth tungstate visible-light-driven photocatalysts, Catal. Sci. Technol., 2012, 2, 694–706).

Zhang et al. have studied the photocatalytic properties of Bi2WO6 micro/nano-structures, including nanoplates, tyre/helix-like structure, disintegrated-flower-like and flower-like superstructures [121,122] These Bi2WO6 micro/nanostructures were found to exhibit different photocatalytic activities under visible light irradiation (Fig. 6). Among these photocatalysts, the uncalcined flower-like Bi2WO6 superstructure possesses the highest photocatalytic performance, while the nanoplates structure shows the lowest activity in the photocatalytic degradation of rhodamine B under visible light irradiation. The

calcination process can be further improved the photocatalytic performance of the flower-like Bi2WO6 superstructure.

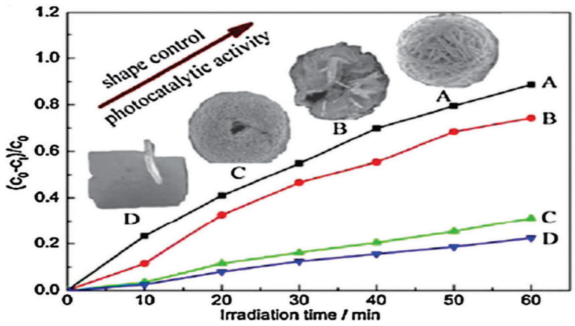

Figure 6. The photocatalytic activities of different Bi_2WO_6 micro/nanostructures: (A) uncalcined flower-like structure, (B) uncalcined disintegrated-flower-like structure, (C) calcined tyre/helix-like structure, (D) uncalcined nanoplates structure [116]. (Reproduced with permission from Liwu Zhang and Yongfa Zhu, A review of controllable synthesis and enhancement of performances of bismuth tungstate visible-light-driven photocatalysts, Catal. Sci. Technol., 2012, 2, 694–706).

2.3 Quaternary photocatalysts

2.3.1 Synthesis of $FeNbO_4$ and Pb_2FeNbO_6 photocatalysts

The $FeNbO_4$ (FNO), Pb_2FeNbO_6 (PFNO) and PFNO: FNO composite photo catalysts were prepared by the conventional solid state reaction method [123-125]. Thus, respective precursors viz. PbO, Fe_2O_3, Bi_2O_3 and Nb_2O_5 were mixed in desired stoichiometric ratio and ground in presence of isopropyl alcohol, and then calcined at required temperature. (i) The pelletized mixture was calcined at 1150 ^oC for 4 hrs to obtain a pure phase monoclinic phase FNO. (ii) The FNO powder obtained in previous step was used. A stoichiometric number of moles of FNO and PbO were mixed and calcined at 800 ^oC for 3 hrs. Further this mixture was pelletized and calcined again at 1125 ^oC for 2 hrs to get PFNO. (iii) A stoichiometric ratio of Pb: Fe: Nb: : 1 : 2 : 2 was mixed. The pelletized mixture was heated at 800 ^oC followed by sintering in the temperature range of 1000-1215 ^oC for more than 24 hrs under static air atmosphere to obtain PFNO: FNO composite system.

2.3.2 Characterization of $FeNbO_4$, and Pb_2FeNbO_6 photocatalysts

The crystal structure of photocatalyst was characterized by X-ray diffractometer. The X-ray diffraction spectra were compared with the standard data in the JCPDS (Joint Committee Powder Diffraction Standards) for identification of the phase. The diffuse

reflectance spectrum (DRS) of the photocatalyst powder was recorded in the wavelength range of 300-800 nm. The X-ray diffraction (XRD) spectra of the photocatalysts viz. FNO, PFNO, and PFNO:FNO indicate the formation of respective phases of monoclinic, cubic and composite systems. XRD spectra for the PFNO:FNO precursors calcined at various temperatures between 1000-1200^{0}C exhibited a mixture of respective PFNO and FNO. However, some impurity peaks were also observed due to Fe_2O_3.

UV-Vis diffuse reflectance spectra of the PFNO:FNO samples calcined at various temperatures exhibit a sharp absorption edge. This absorption edge at still larger wavelength indicates the larger absorption capability of the photocatalyst. The effect of calcination temperature was also observed. The band gap lies in the range of 1.92 eV (PFNO) to 2.04 eV (FNO), the constituent counterparts for PFNO:FNO.

2.3.3 About HfTiErO

High-k gate dielectrics were developed to replace conventional SiO_2 as alternative gate dielectric materials to resolve the problem of device compatibility, reliability and high gate leakage currents [126]. HfO_2 is a suitable high-k gate dielectrics material for integration in complementary metal oxide semiconductor (CMOS) devices because of its good thermal stability and wide band gap on Si [127]. RF sputtering is PVD based technique combined with plasma, it offers a low temperature processing and blocks the oxygen from the ambience, which prevents the formation of interfacial layer (IL) [128]. Therefore, RF sputtering technique explores the possibility of obtaining the good quality high-k gate dielectric thin films, which is the most important requirement of advanced CMOS technology.

2.3.4 Preparation of HfTiErO

Hafnium disk of 99.99% purity with the diameter of 60 mm was used as the sputtering main target, while other targets titanium and erbium were fixed on the main target disk [129]. The sputtering chamber was evacuated with lowest pressure about 3×10^{-4} Pa before Ar and O_2 gases were used. The target was pre-sputtered in argon (Ar) ambient for 10 min in order to remove surface oxide on the target, prior to HfTiErO deposition. During the deposition process, the RF power, substrate temperature, working pressure, substrate-to-target distance, and total gas-flow rate were kept at 100 W, 250 °C, 0.7 Pa, 5.5 cm, and 0.4 ratio, respectively in order to obtain HfTiErO films with different Ti and Er contents. Different Ti and Er materials were introduced on hafnium oxides, after deposition of the ultra-thin films annealed in N_2 atmosphere for 60 s at 500 °C and 700 °C temperatures.

2.3.5 Characterization of HfTiErO

The microstructure and chemical composition of the deposited material were characterized by using atomic force microscopy (AFM) and X-ray photoelectron spectroscopy (XPS).

From AFM, it was concluded that the surface of both as-deposited and annealed films (high-k materials), was very significant because this affects the electrical properties of dielectric thin films and induces shifts in electronic energy levels [130]. It was observed that the surface roughness of films was improved slightly by increasing the erbium concentration. The films display a homogeneous and smooth surface structure, by means of a homogeneous material distribution with a low surface roughness after annealing temperatures at 500 °C and 700 °C. From AFM analysis of both; as deposited and annealed films, it was observed that the root mean square (RMS) surface roughness for S1, S2, S3, S4 and S5 samples are approximately 5.0 nm, 4.0 nm, 3.8 nm, 3.0 nm and 3.2 nm, respectively. The surface of S1 and S2 samples consist of dense narrow spikes in shape, whereas the samples S4 and S5 are more mountain like, flat and void free. Cho *et al*. [131] reported that the amorphous structure of the thin film was changed into the polycrystalline structure after annealing; due to the increase of the grain size, which resulted in an increase of the surface roughness. This shows that the surface of films becomes smoother after annealing process. The diffusion and mobility of the surface atoms can be increased by increasing the annealing temperature, which provides energy to surface atoms. Due to transfer of such atoms to existing voids and defects, the surface gets smoother and as a consequence, the surface roughness is reduced.

From XPS the samples S1, S2, S3, S4 and S5 (S1- $HfTi_6O$, S2- $HfTi_6Er_2O$, S3- $HfTi_6Er_4O$, S4- $HfTi_6Er_4O$ at 500 ℃ and S5- $HfTi_6Er_4O$ at 700 ℃) were analysed. It was observed that a series of peaks from Hf 4f, Er 4d, Hf 4d, C 1s, Ti 2p and O1s arises from the surface contamination of adventitious carbon. Annealing leads to the removal of C 1s peaks for the samples S2 and S4. Effects of experimental charging were corrected by setting the C 1s peak for adventitious carbon at 284.6 eV.

2.3.6 Synthesis of $PbBiO_2Br$ nanosheets samples

Assembly ultrathin $PbBiO_2Br$ nanosheets samples were synthesized using a solvothermal method [132]. In a typical procedure, 0.5 mmol $Bi(NO_3)_3 \cdot 5H_2O$ was added into 20 mL of ethanol containing stoichiometric amounts of hexadecyltrimethylammonium bromide (CTAB) and $Pb(NO_3)_2$ with continuous stirring, and then 5 mL ammonia water was added into this solution. The mixture was stirred for at least 30 min and then poured into a 50 mL teflon-lined stainless autoclave. The autoclave was heated at 180℃ for 12 h under autogenously pressure and then cooled to room temperature. The resulting

precipitates were collected and washed with ethanol and deionized water thoroughly and dried at 70 ℃ in air.

2.3.7 Characterization of $PbBiO_2Br$ nanosheets samples

A novel hierarchical $PbBiO_2Br$ assembled with ultra-thin nanosheets was characterized by scanning electron microscopy (SEM) and transmission electron microscopy (TEM). $PbBiO_2Br$ nanosheets are well-crystallized and have strong absorption in the visible range up to 500 nm. The assembly $PbBiO_2Br$ nanosheets show excellent photocatalytic activity for degradation of organic contaminants under visible light irradiation, which is primarily attributed to the synergistic effect of the high surface area, specially assembled structure and the low recombination rate of charges in the ultrathin nanosheets.

From SEM it was concluded that the sample consists of massive uniform flower like spheres with an average diameter of 2 μm [133, 134]. The spheres are constructed of a large number of nanosheets, which stand almost vertically and connect with each other to form a hierarchical structure. $PbBiO_2Br$ nanosheets are 8~9 nm in thickness, which is consistent with the concept of ultra-thin defined by Cademartiri and Ozin [135].

3. Applications of visible light photoactive catalyst

3.1 Photocatalytic reduction of carbon dioxide

The combustion of fossil fuels leads to the emission of CO_2, which is considered as a main source for global warming caused by the greenhouse effect [136]. Mainly rhenium- and ruthenium-based systems have been reported for their ability to electrochemically or photochemically accelerate the reduction of CO_2 to CO. Carbon monoxide itself can be used as a precursor compound for fuel synthesis processes, where CO and H_2 are mixed as syngas to form hydrocarbons such as methane or methanol [137]. The synthesis and characterisation of the rhenium complex 2 (5, 50-bisphenylethynyl-2, 20-bipyridyl) Re $(CO)_3Cl$ were carried out by Oppelt et al. [138]. Portenkirchner et al. [139] reported that rhenium complex fac-(5, 50-bisphenylethynyl-2, 20-bipyridyl) Re $(CO)_3Cl$ was used as a novel catalyst for the electro- and photochemical reduction of CO_2 to CO in homogeneous solution. (5, 50-Bisphenylethynyl-2, 20-bipyridyl)$Re(CO)_3Cl$ showed a 6.5-fold increase in current density under CO_2 at 1750 mV versus normal hydrogen electrode (NHE) as compared to the operation without CO_2. 2 (2,20-Bipyridyl) Re $(CO)_3Cl$ showed high photocatalytic activity with a quantum yield of 8.7% [140, 141]. The new catalyst 2 (5, 50-bisphenylethynyl-2, 20-bipyridyl) Re $(CO)_3$ Cl showed a 22.8 fold lesser generation of CO under the same conditions as 1 (2,20-bipyridyl) Re $(CO)_3Cl$.

The best estimate for the quantum yield of catalyst 2 (5, 50-bisphenylethynyl-2, 20-bipyridyl) Re $(CO)_3$ Cl (above 360 nm irradiation) is in the order of 0.4%.

3.2 Photocatalytic water splitting

Photocatalytic water splitting is an artificial photosynthesis process. In this process, a photoelectrochemical cell is used for the dissociation of water into its constituents, hydrogen and oxygen, using either artificial or natural light. Photocatalytic water splitting has the simplicity of using a powder in solution and sunlight to produce H_2 and O_2 from water and it can provide a clean, renewable energy, without producing greenhouse gases or having many adverse effects on the atmosphere.

Photocatalytic water splitting has been investigated to produce hydrogen fuel, which burns cleanly and can be used in a hydrogen fuel cell. Water splitting is beneficial since it utilizes water, an inexpensive renewable resource.

When H_2O is split into O_2 and H_2, the stoichiometric ratio of its products is 2:1:

$$2\ H_2O \overset{\text{photon energy} > 1.23eV}{\rightleftharpoons} 2\ H_2 + O_2$$

The process of water splitting is a highly endothermic process ($\Delta H > 0$). Water splitting occurs naturally in photosynthesis when photon energy is absorbed and converted into the chemical energy through a complex biological pathway. Production of hydrogen from water requires large amounts of input energy, making it incompatible with existing energy generation. For this reason, most of commercially produced hydrogen gas is from natural gas.

Three significant properties of water splitting photocatalysts are (i) Crystal structure and its thermodynamic phase stability (versus competing solids and gases); (ii) Band gap; and (iii) Conduction band (CB) and valence band (VB) edge positions relative to the H_2/H_2O and O_2/H_2O levels in water.

$NaTaO_3$: La yields the highest water splitting rate by photocatalysts without using sacrificial reagents [142]. This UV-based photocatalyst was shown to be highly effective with water splitting rates of 9.7 mmol h^{-1} and a quantum yield of 56%. The nanostep structure of the material promotes water splitting as edges functioning as H_2 production sites and the grooves functioning as O_2 production sites. Addition of NiO particles as co-catalysts assisted in H_2 production; this step was done by using an impregnation method with an aqueous solution of $Ni(NO_3)_2 \cdot 6H_2O$ and evaporating the solution in the presence of the photocatalyst. NaTaO 3 has a conduction band higher than that of NiO, so

photogenerated electrons are more easily transferred to the conduction band of NiO for H_2 evolution [143].

$K_3Ta_3B_2O_{12}$ has the ability to split water without the assistance of co-catalysts and gives a quantum yield of 6.5% along with a water splitting rate of 1.21 mmol h^{-1}. This ability is due to the pillared structure of the photocatalyst, which involves TaO_6 pillars connected by BO_3 triangle units. Loading with NiO did not assist the photocatalyst due to the highly active H_2 evolution sites [144]. GaN, Ge_3N_4 and Ta_3N_5 are known water splitting photocatalysts [145, 146]. The band edge positions have been experimentally measured only for Ta_3N_5 [147]. Zr_2ON_2 has been reported as a promising material for photoelectrochemical water splitting [148]. Cu_3N, AgN_3, and Zr_3N_4 are known compounds but these have not been reported as photocatalysts yet. $Ti_3O_3N_2$ has the potential to be better water splitting photocatalysts than TaON. $Na_4WO_2N_2$ and $Ca_5WO_2N_4$ have a band gap too large for visible light absorption and can work under UV light illumination.

3.3 Photocatalytic pervious concrete with TiO_2 and paints

Direct interaction of TiO_2 with UV light is very critical. Mixing TiO_2 into traditional concrete can only have limited NO_x reduction effectiveness at the air/solid interface. The process was observed to improve after the concrete material was abraded (some cement paste was peeled off and more TiO_2 was exposed at the surface) [149]. The durability of the photocatalytic effect becomes another challenge if TiO_2 is applied to highly trafficked highways through surface material adhesion. The dynamic tire-pavement interaction under shear and abrasion impact can dislodge coated TiO_2 particles at the surface, leaving untreated pavements. Therefore, coating TiO_2 on the substrate of pervious concrete could have a number of benefits, to maximize the effect of air purification in pavements through the TiO_2 photocatalytic reaction. As compared to traditional concrete pavements which have low porosities and relatively smooth surface textures, pervious concrete pavements have much higher porosities and rougher surface features. The higher void ratio and the increased concave surface texture (due to surface voids) with more surface area could enhance the bonding and durability of the applied TiO_2 at the surface, reduce impacts due to traffic abrasion and climate (snow, ice, water, heat, etc.), and increase the direct contact between TiO_2 and natural light. At the same time, pervious concrete pavement allows water to infiltrate completely through it so that rainwater can filter into the ground and replenish groundwater resources [150]. Installing pervious concrete may reduce costs in installing drainage and storm water systems, reduce the urban heat island effect and noise, improve roadway skid resistance, and prevent hydroplaning. TiO_2 treated pervious concrete pavement can be widely used for pedestrian sidewalks, bike

lanes, parking lots, roadway shoulders, and urban low traffic streets for its storm water benefits and air quality purification, resulting in a greener urban living environment.

Two most effective coatings, the commercial water-based TiO_2 (CWB) and the driveway protector mix (DPM), were painted on sections of an actual newly paved pervious concrete sidewalk located between two sports playfields in Pullman, Washington for scaling observation. The sidewalk endured the same type of weathering at the same time of year as the weathering samples. Both coatings were painted on two different 2 x 2 ft. areas each for observation. The DPM coating adds an obvious white color to the pavement, while the CWB coating turns the pavement to slightly lighter gray.

Both coatings had faded in colour with time. After 3 months, the appearance of the CWB coating was not as distinguishable from the regular uncoated pervious concrete as it was originally. The DPM coating, though slightly more faded than it was originally, still had a white colour. The white colour of the DPM coating indicates that the coating is still there and still working to effectively remove pollutants, whereas with the CWB coating, it is unknown whether the coating has come off due to abrasive forces or if it is still working. If these coatings were applied in the field, the DPM coating could be reapplied as a maintenance fulfillment, whenever it was obvious that the colour had worn away.

3.4 Photocatalytic materials for environmental remediation

Due to the position of the valence band of ZnO, the photogenerated holes have strong enough oxidizing power to decompose most of the organic compounds [143]. ZnO has been used to decompose aqueous solutions of several dyes [152], and many other environmental pollutants [153]. Chen et al. [154] reported that ZnO is more efficient than TiO_2 because of its good optoelectronic, catalytic and photochemical properties along with its low cost.

Cu_2O octahedra show better photocatalytic activity than cubes, because the {1 1 1} facets are more active than {1 0 0} facets due to the dangling bonds of {1 1 1} surfaces, whilst {1 0 0} facets have saturated chemical bonds and no dangling bands exist [155, 156]. Huang et al. [157] prepared Cu_2O nanoparticles and microparticles for the photodegradation of methyl orange. Nanoporous WO_3 films anodically grown on tungsten foil substrates were photoactive for the oxidation of methylene blue and the reductive conversion of Cr(VI) under visible light illumination [158]. WO_3 films deposited on a Pt substrate showed a higher photoelectrocatalytic activity for the photodegradation of naphthol blue black than TiO_2 nanoparticulate film electrodes [159].

Bessekhouad et al. [160] found that Bi_2O_3 was able to degrade orange II but the efficiency of the photocatalytic reaction was rather low. Monoclinic α-Bi_2O_3, synthesized

via calcination of hydrothermally prepared $(BiO)_2CO_3$ was much more active than commercial Bi_2O_3 for the degradation of NO and formaldehyde at typical indoor air concentration [161].

The research on ternary and quaternary oxides is an efficient strategy to overcome the intrinsic limitations of the binary metal oxides and new materials have been obtained, which are suitable to exploit the visible component of sunlight. Kohtani et al. [162] reported that $BiVO_4$ can efficiently decompose long-chain alkyl phenols and polycyclic aromatic hydrocarbons under visible light irradiation. Ag_3VO_4 powders synthesized by precipitation [163] were evaluated for the decolorization of acid red B under visible light irradiation. $CdWO_4$ is investigated for the photodegradation of organic compounds under UV light irradiation [164,165]. Monoclinic $CdWO_4$ short rods synthesized via a hydrothermal process exhibited a high photocatalytic activity for the degradation of methyl orange and rhodamine B [164].

Single-phase quaternary oxide materials have been recently studied with the aim to develop novel photocatalysts showing high activity in the visible light region. Shan et al. [106] tested layered Bi-based oxyhalides for the degradation of methyl orange under UV and visible illumination. Bi_4NbO_8Cl (Eg = 2.38 eV) showed an excellent visible light efficiency and was more active than the ternary oxychloride Bi_3O_4Cl (Eg = 2.80 eV) [166].

4. Conclusion

TiO_2 nanocrystallites are uniformly dispersed throughout the amorphous SiO_2 matrix, and nanopores form on top of TiO_2 particles, resulting in an improved photoactivity through increasing the effective absorption sites. The specific surface areas and the surface states of the binary films decrease gradually with increasing annealing temperature; thus, deteriorating the photocatalytic activity after annealing. With the onset of the photocatalytic activity for NO_x abatement is concomitant to the switch between amorphous to a crystalline phase with an electronic band gap within 3.05–3.10 eV, where the most active photocatalyst revealed predominantly rutile phase together with anatase as the minority phase.

The ternary semiconductor hybrid prepared by calcination of $KTaO_3$, CdS and MoS_2 powders at the 10:5:1 molar ratio exhibited very good stability in toluene degradation and excellent photocatalytic performance in phenol degradation among all obtained photocatalysts. The activity reached 80% under UV-Vis and 42% under Vis light 60 min irradiation. This relatively high photoactivity under visible light is due to the presence of heterojunction between semiconductors.

GTF exhibited a higher photocatalytic activity during the degradation of rhodamine B as compared to the unsupported TiO_2–Fe_3O_4 composite and pure TiO_2 NPs. The electron transfer between the TiO_2 NPs and RGO help in achieving the high durability of GTF. GTF can be easily recollected from water using a magnet. Due to its attractive features such as easy recollection and reusability, the GTF hybrid nanocomposite is used in wastewater treatment.

The Bi_2WO_6 nanoplates showed high activity as photocatalysts under visible light irradiation. Quaternary photocatalyst (Pb_2FeNbO_6) show significant photocatalytic activity for methylene blue degradation due to its suitable band energetics. The composite photocatalyst (Pb_2FeNbO_6) is found to be twice efficient than $TiO_{2-x}N_x$. XPS Hf 4f and O1 s results shows that ultra-thin HfTiErO films microstructure is formed, while the annealed temperature also affected the microstructures that caused the increase in intensity and binding energy. These improved material and electrical results indicate that HfTiErO may be used for the generation of higher-k gate dielectrics. The electrocatalytic activity of the new compound 2 (5, 50-bisphenylethynyl-2, 20-bipyridyl) Re $(CO)_3$ Cl is in the range of 45% for Faradaic efficiency for CO formation and ranks equally with the benchmark molecule 1 (2,20-bipyridyl) Re $(CO)_3Cl$.

References

[1] E.J. Weber, R.L. Adams, Chemical and sediment mediated reduction of the azo dye: Disperse blue 79, Environ. Sci. Technol. 29 (1995) 1163-1170. https://doi.org/10.1021/es00005a005

[2] C. Wang, A. Yediler, D. Linert, Z. Wang, A. Kettrup, Toxicity evaluation of reactive dye stuff, auxiliaries and selected effluents in textile finishing industry to luminescent bacteria vibrio fisheri, Chemosphere 46 (2002) 339-344. https://doi.org/10.1016/S0045-6535(01)00086-8

[3] W.C. Tincher, J.R. Robertson, Analysis of dyes in textile dyeing waste water, Text. Chem. Color. 43 (1982) 269-275.

[4] World Health Organization, Phenol: Environmental Health Criteria 161, World Health Organization: Geneva, Switzerland (1994).

[5] World Health Organization, Cresols: Environmental Health Criteria 168, World Health Organization: Geneva, Switzerland (1995).

[6] European Union. The list of priority substances in the field of water policy and amending directive, Council directive 2455/2001/ECC. Official Journal of the European Communities L331, 20 November 2001, 1–5.

[7] Environment Canada, The Second Priority Substances List (PSL2) of the Canadian Environmental Protection Act (CEPA), Environment Canada: Gatineau, Canada (1995).

[8] United States Environmental Protection Agency (USEPA), Sampling and Analysis Procedure for Screening of Industrial Effluents for Priority Pollutants, Environment Monitoring and Support Laboratory: Cincinnati, OH, USA (1977).

[9] F.M. Pfeffer, The 1977 screening survey for measurement of organic priority pollutants in petroleum refinery wastewaters, ASTM Specif. Tech. Publ. 686 (1979) 181–190. https://doi.org/10.1520/STP35014S

[10] L.H. Keith, Identification of organic compounds in unbleached treated kraft paper mill wastewaters, Environ. Sci. Technol. 10 (1976) 555–564. https://doi.org/10.1021/es60117a009

[11] B.R. Parkhurst, A.S. Bradshaw, J.L. Forte, An evaluation of the acute toxicity to aquatic biota of a coal conversion effluent and it major components, Bull. Environ. Contam. Toxicol. 23 (1979) 349–356. https://doi.org/10.1007/BF01769968.

[12] G. Jungclaus, V. Avila, R. Hites, Organic compounds in an industrial wastewater: A case study of their environmental impact, Environ. Sci. Technol. 12 (1978) 88–96. https://doi.org/10.1021/es60137a015

[13] I. Kamenev, R. Munter, L. Pikkov, L. Kekisheva, Wastewater treatment in oil shale chemical industry, Oil Shale 20 (2003) 443–457.

[14] Z. Guo, R. Ma, G. Li, Degradation of phenol by nanomaterial TiO_2 in wastewater, Chem. Eng. J. 119 (2006) 55–59. https://doi.org/10.1016/j.cej.2006.01.017

[15] M. Auriol, Y. Filali-Meknassi, R.D. Tyagi, C.D. Adams, R.Y. Surampalli, Endocrine disrupting compounds removal from wastewater, a new challenge, Process Biochem. 41 (2006) 525–539. https://doi.org/10.1016/j.procbio.2005.09.017

[16] P.R. Gogate, A.B. Pandit, A review of imperative technologies for wastewater treatment I: oxidation technologies at ambient conditions, Adv. Environ. Res. 8 (2004) 501–551. https://doi.org/10.1016/S1093-0191(03)00032-7

[17] K.H. Wang, Y.H. Hsieh, L.J. Chen, The heterogeneous photocatalytic degradation, intermediates and mineralization for the aqueous solution of cresols and nitrophenols, J. Hazard. Mater. 59 (1998) 251–260. https://doi.org/10.1016/S0304-3894(97)00151-9

[18] Matilainena, M. Sillanpaa, Removal of natural organic matter from drinking water by advanced oxidation processes, Chemosphere 80 (2010) 351–365. https://doi.org/10.1016/j.chemosphere.2010.04.067

[19] W.H. Glaze, J.W. Kang, D.H. Chapin, Chemistry of water treatment processes involving ozone, hydrogen peroxide and ultraviolet radiation, Ozone Sci. Eng. 9 (1987) 335–352. https://doi.org/10.1080/01919518708552148

[20] K.Y. Jung, S.B. Park, Photoactivity of SiO_2\$TiO_2$ and ZrO_2\$TiO_2$ mixed oxide prepared by sol-gel method, Mater. Lett. 58 (2004) 2897-2900. https://doi.org/10.1016/j.matlet.2004.05.015

[21] Ch. Guillard, B. Beaugiraud, C. Dutriez, Physicochemical properties and photocatalytic activities of TiO_2-films prepared by sol-gel methods, Appl. Catal. B: Environ. 39(4) (2002) 331-342. https://doi.org/10.1016/S0926-3373(02)00120-0

[22] S.H. Oh, D. Jin Kim and S.H. Hahn, Comparison of optical and photocatalytic properties of TiO_2 thin films prepared by electron-beam evaporation and sol–gel dip-coating, Mater. Lett. 57, 4151-4155 (2003). https://doi.org/10.1016/S0167-577X(03)00281-7

[23] Y.R. Do, W. Lee, K. Dwight, A. Wold, The effect of WO_3 on the photocatalytic activity of TiO_2, J. Solid State Chem. 108 (1994) 198-201. https://doi.org/10.1006/jssc.1994.1031

[24] J. Papa, S. Soled, K. Dwight, A. Wold, Surface acidity and photocatalytic activity of TiO_2, WO_3/TiO_2, and MoO_3/TiO_2 photocatalysts, Chem. Mater 1994, 6, 496-500. https://doi.org/10.1021/cm00040a026

[25] Y. Oasawa, A. Gratzel, Effect of surface hydroxyl density on photocatalytic oxygen generation in aqueous TiO_2 suspensions, J. Chem. Soc., Faraday Trans.1 84(1) (1998) 197-205. https://doi.org/10.1039/f19888400197

[26] E. Ozensoy, J. Szanyi, C.H.F. Peden, Model NO_x storage systems: storage capacity and thermal aging of BaO/ θ-Al_2O_3/NiAl (1 0 0), J. Catal. 243 (2006) 149–157. https://doi.org/10.1016/j.jcat.2006.06.028

[27] E. Kayhan, S. M. Andonova, G.S. Senturk, C.C. Chusuei, E. Ozensoy, Iron promoted NO_x storage materials: Structural properties and NO_x uptake, J. Phys. Chem. C 114 (2010) 357–369. https://doi.org/10.1021/jp907982q

[28] E. Emmez, E.I. Vovk, V.I. Bukhtiyarov, E. Ozensoy, Direct evidence for the instability and deactivation of mixed-oxide systems: Influence of surface

segregation and subsurface diffusion, J. Phys. Chem. C 115 (2011) 22438–22443. https://doi.org/10.1021/jp206969h

[29] H. Zhang, Y. Zhu, Significant visible photoactivity and antiphotocorrosion performance of CdS photocatalysts after monolayer polyaniline hybridization, J. Phys. Chem. C 114 (2010) 5822–5826. https://doi.org/10.1021/jp910930t

[30] M. Zhong, J. Shi, F. Xiong, W. Zhang, C. Li, Enhancement of photoelectrochemical activity of nanocrystalline CdS photoanode by surface modification with TiO_2 for hydrogen production and electricity generation, Sol. Energy 86 (2012) 756–763. https://doi.org/10.1016/j.solener.2011.12.006

[31] X. Li, T. Xia, C. Xu, J. Murowchick, X. Chen, Synthesis and photoactivity of nanostructured CdS–TiO_2 composite catalysts, Catal. Today 225 (2014) 64–73. https://doi.org/10.1016/j.cattod.2013.10.086

[32] D. He, M. Chen, F. Teng, G. Li, H. Shi, J. Wang, M. Xu, T. Lu, X. Ji, Y. Lv, Enhanced cyclability of CdS/TiO_2 photocatalyst by stable interface structure, Superlattices Microstruct. 51 (2012) 799–808. https://doi.org/10.1016/j.spmi.2012.03.026

[33] S. Panigrahi, D. Basak, Morphology driven ultraviolet photosensitivity in ZnO–CdS composite, J. Colloid Interface Sci. 364 (2011) 10–17. https://doi.org/10.1016/j.jcis.2011.08.001

[34] T.K. Jana, A. Pal, K. Chatterjee, Self-assembled flower like CdS–ZnO nanocomposite and its photo catalytic activity, J. Alloys Compd. 583 (2014) 510–515. https://doi.org/10.1016/j.jallcom.2013.08.184

[35] S. Liu, H. Li, L. Yan, Synthesis and photocatalytic activity of three-dimensional ZnS/CdS composites, Mater. Res. Bull. 48 (2013) 3328–3334. https://doi.org/10.1016/j.materresbull.2013.05.055

[36] X. Liu, Y. Yan, Z. Da, W. Shi, C. Ma, P. Lv, Y. Tang, G. Yao, Y. Wu, P. Huo, Significantly enhanced photocatalytic performance of CdS coupled WO_3 nanosheets and the mechanism study, Chem. Eng. J. 214 (2014) 243–250. https://doi.org/10.1016/j.cej.2013.12.058

[37] X. Zong, H. Yan, G. Wu, G. Ma, F. Wen, L. Wang, C. Li, Enhancement photocatalytic H_2 evolution on CdS by loading MoS_2 as co-catalyst under visible light irradiation, J. Am. Chem. Soc. 130 **(**2008) 7176–7177. https://doi.org/10.1021/ja8007825

[38] D.W. Bahnemann, D. Bockelmann, R. Goslich, M. Hilgendorff, D. Weichgrebe, in: D.F. Ollis et al. (Eds.), Photocatalytic purification and treatment of water and air, Elsevier, Amsterdam 22 (1993) 301-320.

[39] G.N. Schrauzer, T.D. Guth, Photocatalytic reactions: Photolysis of water and photoreduction of nitrogen on titanium dioxide, J. Am. Chem. Soc. 99(22) (1977) 7189-7193. https://doi.org/10.1021/ja00464a015

[40] M.I. Litter, J.A. Navio, Comparison of the photocatalytic efficiency of TiO_2, iron oxides and mixed Ti (IV) and Fe (III) oxides: Photodegradation of oligocarboxylic acids, J. Photochem. Photobiol. A: Chem. 84(2) (1994) 183-193. https://doi.org/10.1016/1010-6030(94)03858-9

[41] L. Palmisano, M. Schiavello, A. Sclafani, C. Martin, I. Martin, V. Rives, Surface properties of iron-titania photocatalysts employed for 4-nitrophenol photodegradation in aqueous TiO_2 dispersion, Catal. Lett. 24 (3-4) (1994) 303-315. https://doi.org/10.1007/BF00811803

[42] W. Choi, A. Termin, M.R Hoffmann, Role of metal-ion dopants in quantum-sized TiO_2 co-relation between photoreactivity and charge-carrier recombination dynamics, J. Phys. Chem. 98 (1994) 13669-13679. https://doi.org/10.1021/j100102a038

[43] J.A. Navio, G. Colon, M.I. Litter, G.N. Bianco, Synthesis, characterization and photocatalytic properties of iron-doped titania semiconductors prepared from TiO_2 and iron (III) acetylacetonate, J. Mol. Catal. A. Chem. 106(3) (1996) 267-276. https://doi.org/10.1016/1381-1169(95)00264-2

[44] M. Anpo, M. Che, Applications of photoluminescence techniques to the characterization of solid surfaces in relation to adsorption, catalysis, and photocatalysis, Adv. Catal. 44 (2000) 119-257. https://doi.org/10.1016/S0360-0564(08)60513-1

[45] M. Anpo, M. Tomonari, M.A. Fox, In situ photoluminescence of titania as a probe of photocatalytic reactions, J. Phys. Chem. 93(21) (1989) 7300-7302. https://doi.org/10.1021/j100358a008

[46] M.A. Fox, M.T. Dulay, Heterogeneous photocatalysis, Chem. Rev. 93(1) (1993) 341-357. https://doi.org/10.1021/cr00017a016

[47] S.-I. Nishimoto, B. Ohtani, H. Kajiwara, T. Kagiya, Correlation of the crystal structure of titanium dioxide prepared from titanium tetra-2-propoxide with the photocatalytic activity for redox reactions in aqueous propan-2-ol and silver salt

solutions, J. Chem. Soc. Faraday Trans. I, 81 (1985) 61-68. https://doi.org/10.1039/f19858100061

[48] J. Yang, J. H. Swisher, The phase stabilization of $Zn_2Ti_3O_8$, Mater. Charact. 37 (1996) 153-159. https://doi.org/10.1016/S1044-5803(96)00098-8

[49] C. Wang, J. Zhao, X. Wang, B. Mai, G. Sheng P. Peng J. Fu, Preparation, characterization and photocatalytic activity of nano-sized ZnO/SnO_2 coupled photocatalysts, Appl. Catal., B: Environ. 39 (2002) 269–279. https://doi.org/10.1016/S0926-3373(02)00115-7

[50] S. Liao, D. Huang, D. Yu, Y. Su, G. Yuan, Preparation and characterization of ZnO/TiO_2, SO_4^{2-}/ZnO/TiO_2 photocatalyst and their photocatalysis, J. Photochem Photobiol., A: Chem. 168 (2004) 7-13. https://doi.org/10.1016/j.jphotochem.2004.05.010

[51] J.T. Zhang, Z.G. Xiong, X. S. Zhao, Graphene–metal–oxide composites for the degradation of dyes under visible light irradiation, J. Mater. Chem. 21 (2011) 3634–3640. https://doi.org/10.1039/c0jm03827j

[52] C. Chen, W.M. Cai, M.C. Long, B.X. Zhou, Y.H. Wu, D.Y. Wu, Y.J. Feng, Synthesis of visible-light responsive graphene oxide/TiO_2 composites with p/n heterojunction, ACS Nano 4(11) (2010) 6425–6432. https://doi.org/10.1021/nn102130m

[53] Y. Lin, Z. Geng, H. Cai, L. Ma, J. Chen, J. Zeng, N. Pan, X. Wang, Ternary graphene–TiO_2–Fe_3O_4 nanocomposite as a recollectable photocatalyst with enhanced durability, Eur. J. Inorg. Chem. 28 (2012) 4439–4444. https://doi.org/10.1002/ejic.201200454

[54] Castro, P. Begue, B. Jimenez, J. Ricote, R. Jimenez, J. Galy, New $Bi_2Mo_{1-x}W_xO_6$ solid solution: Mechanosynthesis, structural study, and ferroelectric properties of the x = 0.75 member, Chem. Mater. 15(17) (2003) 3395-3401. https://doi.org/10.1021/cm030224r

[55] S. Luo, Y. Noguchi, M. Miyayama, T. Kudo, Rietveld analysis and dielectric properties of Bi_2WO_6–$Bi_4Ti_3O_{12}$ ferroelectric system, Mater. Res. Bull. 36 (2001) 531-540. https://doi.org/10.1016/S0025-5408(01)00516-5

[56] H.B. Fu, C.S. Pan, W.Q. Yao, Y.F. Zhu, Visible-light-induced degradation of rhodamine B by nanosized Bi_2WO_6, J. Phys. Chem. B 109(47) (2005) 22432-22439. https://doi.org/10.1021/jp052995j

[57] C. Zhang, Y.F. Zhu, Synthesis of square Bi_2WO_6 nanoplates as high-activity visible-light-driven photocatalysts, Chem. Mater. 17(13) (2005) 3537-3545. https://doi.org/10.1021/cm0501517

[58] J.W. Tang, Z.G. Zou, J.H. Ye, Photocatalytic decomposition of organic contaminants by Bi_2WO_6 under visible light irradiation, Catal. Lett. 92(1-2) (2004) 53-56. https://doi.org/10.1023/B:CATL.0000011086.20412.aa

[59] T.S. Natarajan, H.C. Bajaj, R.J. Tayade, Synthesis of homogeneous sphere-like Bi_2WO_6 nanostructure by silica protected calcination with high visible-light-driven photocatalytic activity under direct sunlight, Cryst .Eng. Comm. 17(5) (2015) 1037-1049. https://doi.org/10.1039/C4CE01839G

[60] R.J. Tayade, H.C. Bajaj, R.V. Jasra, Photocatalytic removal of organic contaminants from water exploiting tuned bandgap photocatalysts, Desalination 275(1) (2011) 160-165. https://doi.org/10.1016/j.desal.2011.02.047

[61] T.K. Pathak, N.H. Vasoya, T.S. Natarajan, K.B. Modi, R.J. Tayade, Photocatalytic degradation of aqueous nitrobenzene solution using nanocrystalline Mg-Mn ferrites, Materials Sci. Forum 764 (2013) 116-129. https://doi.org/10.4028/www.scientific.net/MSF.764.116

[62] S. Sadhu, A. Patra, Lattice strain controls the carrier relaxation dynamics in $Cd_xZn_{1-x}S$ alloy quantum dots, J. Phys. Chem. C 116(28) (2012) 15167–15173. https://doi.org/10.1021/jp304901w

[63] X. Zhong, Y. Feng, Y. Zhang, Z. Gu, L. Zou, A facile route to violet- to orange-emitting $Cd_xZn_{1-x}Se$ alloy nanocrystals via cation exchange reaction, Nanotechnol. 18(38) (2007) 385606-385612. https://doi.org/10.1088/0957-4484/18/38/385606

[64] L.Y. Chen, P.A. Yang, C.H. Tseng, B.J. Hwang, C.H. Chen, Internal structure of tunable ternary $CdSe_xS_{1-x}$ quantum dots unraveled by X-ray absorption spectroscopy, App. Phys. Lett. 100(16) (2012) 163113-16116. https://doi.org/10.1063/1.3703123

[65] G. Kartopu, A.J. Clayton, W.S.M. Brooks, S.D. Hodgson, V. Barrioz, A. Maertens, D.A. Lamb, S.J.C. Irvine, Effect of window layer composition in $Cd_{1-x}Zn_xS$/CdTe solar cells, Prog. Photovolt. Res. 22(1) (2012) 18-23. https://doi.org/10.1002/pip.2272

[66] X. Wu, Y. Yu, Y. Liu, Y. Xu, C. Liu, B. Zhang, Synthesis of hollow $Cd_xZn_{1-x}Se$ nanoframes through the selective cation exchange of inorganic–organic hybrid

ZnSe–amine nanoflakes with cadmium ions, Angew. Chem. Int. Ed. 51(13) (2012) 3211–3215. https://doi.org/10.1002/anie.201108098

[67] C.I. Wang, Z. Yang, A.P. Periasamy, H.T. Chang, Photoluminescent C-dots RGO probe for sensitive and selective detection of acetylinecholine, Anal. Chem. 85(6) (2013) 3263-3270. https://doi.org/10.1021/ac303613d

[68] W.A. Tisdale, K.J. Williams, B.A. Timp, D.J. Norris, E.S. Aydil, X.Y. Zhu, Hot-electron transfer from semiconductor nanocrystals, Science 328 (2010) 1543–1547. https://doi.org/10.1126/science.1185509

[69] P. Aguiar, D. Chadwick, L. Kershenbaum, Modelling of an indirect internal reforming solid oxide fuel cell, Chem. Eng. Sci. 57 (2002) 1665–1677. https://doi.org/10.1016/S0009-2509(02)00058-1

[70] Q. Deng, S.L. Jiang, T.J. Cai, Z.S. Peng, Z.J. Fang, Selective oxidation of isobutane over $H_xFe_{0.12}Mo_{11}VPAs_{0.3}O_y$ heteropoly compound catalyst, J. Mol. Catal. A: Chem. 229 (2005) 165–170. https://doi.org/10.1016/j.molcata.2004.11.013

[71] T.J. Cai, M. Yue, X.W. Wang, Q. Deng, Z.S. Peng, W.H. Zhou, Preparation, characterization and photocatalytic performance of $NdPW_{12}O_{40}/TiO_2$ composite catalyst, Chin. J. Catal. 28(1) (2007) 10–16. https://doi.org/10.1016/S1872-2067(07)60007-2

[72] X.J. Wu, Y.C. Liao, X.W. Wang, Z.S. Peng, Y.H. Jiang, X.Y. Liu, T.J. Cai, Microwave solid-phase synthesis of bismuth phosphotungstate nanoparticle catalysts and photocatalytic elimation of methanol, Acta Sci. Circumst. 28(5) (2008) 965–970.

[73] Q. Deng, W.H. Zhou, M. X. Li, Z.S. Peng, S.L. Jiang, M. Yue, T.J. Cai, Microwave radiation solid-phase synthesis of phosphotungstate nanoparticle catalysts and photocatalytic degradation of formaldehyde, J. Mol. Catal. A: Chem. 262 (2007) 149–155. https://doi.org/10.1016/j.molcata.2006.08.043

[74] H. Xue, Z.H. Li, L. Wu, Z.X. Ding, X.X. Wang, X.Z. Fu, Nanocrystalline ternary wide band gap p-block metal semiconductor $Sr_2Sb_2O_7$: Hydrothermal synthesis and photocatalytic benzene degradation, J. Phys. Chem. C 112(15) (2008) 5850-5855. https://doi.org/10.1021/jp712186r

[75] Z. G. Yi, J.H. Ye, N. Kikugawa, T. Kako, S.X. Ouyang, H. Stuart-Williams, H. Yang, J.Y. Cao, W.J. Luo, Z.S. Li, Y. Liu, R. Withers, An orthophosphate

semiconductor with photooxidation properties under visible-light irradiation, Nat. Mater. 9 (2010) 559-564. https://doi.org/10.1038/nmat2780

[76] N. Umezawa, S.X. Ouyang, J.H. Ye, Theoretical study of high photocatalytic performance of Ag_3PO_4, Phys. Rev. B 83(3-1) (2011) 035202.

[77] X.C. Wang, K. Maeda, A. Thomas, K. Takanabe, G. Xin, J.M. Carlsson, K. Domen, M. Antonietti, A metal-free polymeric photocatalyst for hydrogen production from water under visible light, Nat. Mater. 8 (2009) 76-80. https://doi.org/10.1038/nmat2317

[78] C.S. Pan, J. Xu, Y.J. Wang, D. Li, Y.F. Zhu, Dramatic activity of $C_3N_4/BiPO_4$ photocatalyst with core/shell structure formed by self-assembly, Adv. Funct. Mater. 22(7) (2012) 1518-1524. https://doi.org/10.1002/adfm.201102306

[79] Q.J. Xiang, J.G. Yu, M. Jaroniec, Preparation and enhanced visible-light photocatalytic H_2-production activity of graphene/C_3N_4 composites, J. Phys. Chem. C 115 (2011) 7355-7363. https://doi.org/10.1021/jp200953k

[80] L. Ge, C.C. Han, J. Liu, Novel visible light-induced g-C_3N_4/Bi_2WO_6 composite photocatalysts for efficient degradation of methyl orange, Appl. Catal. B 108-109 (2011) 100-107. https://doi.org/10.1016/j.apcatb.2011.08.014

[81] G. Shiravand, A. Badiei, G.M. Ziarani, M. Jafarabadi, M. Hamzehloo, Photocatalytic synthesis of phenol by direct hydroxylation of benzene by modified nanoporous silica (LUS-1) under sunlight, Chin. J. Catal. 33 (2012) 1347-1353. https://doi.org/10.1016/S1872-2067(11)60422-1

[82] H. Pan, X. K. Li, Z. J. Zhuang, C. Zhang, g-C_3N_4/SiO_2–HNb_3O_8 composites with enhanced photocatalytic activities for rhodamine B degradation under visible light, J. Mol. Catal. A: Chem 345(1-2) (2011) 90-95. https://doi.org/10.1016/j.molcata.2011.05.024

[83] S.C. Yan, S.B. Lv, Z.S. Li, Z.G. Zou, Organic–inorganic composite photocatalyst of g-C_3N_4 and TaON with improved visible light photocatalytic activities, Dalton Trans. J. Inorg. Chem. 39 (2010) 1488-1491. https://doi.org/10.1039/B914110C

[84] K. Shen, M.A. Gondal, R.G. Siddique, S. Shi, S. Wang, J. Sun, Q. Xu, Preparation of ternary Ag/Ag_3PO_4/g-C_3N_4 hybrid photocatalysts and their enhanced photocatalytic activity driven by visible light, Chin. J. Catal. 35 (2014) 78–84. https://doi.org/10.1016/S1872-2067(12)60712-8

[85] H.I. Kim, J. Kim, W. Kim, W. Choi, Enhanced photocatalytic and photoelectrochemical activity in the ternary hybrid of CdS/TiO_2/WO_3 through the

cascadal electron transfer, J. Phys. Chem. C. 115 (2011) 9797–9805. https://doi.org/10.1021/jp1122823

[86] C.J. Lin, Y.T. Lu, C.H. Hsieh, S.H. Chien, Surface modification of highly ordered TiO_2 nanotube arrays for efficient photoelectrocatalytic water splitting, Appl. Phys. Lett. 94 (2009) 113102-113110. https://doi.org/10.1063/1.3099338

[87] C. Chen, Y. Xie, G. Ali, S.H. Yoo, S.O. Cho, Improved conversion efficiency of CdS quantum dots-sensitized TiO_2 nanotube array using ZnO energy barrier layer, Nanotechnol. 22 (2011) 015202-015210. https://doi.org/10.1088/0957-4484/22/1/015202

[88] A.J. Bwamba, N. Alu, A.K. Kenneth, Z. Abdullahi, I.U. Unwana, C.E. Augustine, O.A. Anthony, Characterization of CZTS absorbent material prepared by field assisted spray pyrolysis, Am. J. Mater. Sci. 4 (2014) 127-132.

[89] L.Y. Yeh, K.W. Cheng, Preparation of the Ag-Zn-Sn-S quaternary photoelectrodes using chemical bath deposition for photoelectrochemical applications, Thin Solid Films 558 (2014) 289-293. https://doi.org/10.1016/j.tsf.2014.02.046

[90] Z. Zou, J. Ye, K. Sayama, H. Arakawa, Direct splitting of water under visible light irradiation with an oxide semiconductor photocatalyst, Nature 414 (2001) 625-627. https://doi.org/10.1038/414625a

[91] Kudo, H. Kato, Photocatalytic decomposition of water into H_2 and O_2 over novel photocatalyst $K_3Ta_3Si_2O_{13}$ with pillared structure consisting of three TaO_6 chains, Chem. Lett. 20 (1997) 867-868. https://doi.org/10.1246/cl.1997.867

[92] Ishikawa, T. Takata, J.N. Kondo, M. Hara, H. Kobayashi, K. Domen, K., Oxysulfide $Sm_2Ti_2S_2O_5$ as a stable photocatalyst for water oxidation and reduction under visible light irradiation ($\lambda \leq 650$ nm), J. Am. Chem. Soc. 124(45) (2002) 13547-13553. https://doi.org/10.1021/ja0269643

[93] R. Asahi, T. Morikawa, T. Ohwaki, K. Aoki, Y. Taqo, Visible-light photocatalysis in nitrogen-doped titanium oxides, Sci. 293 (2001) 269-71. https://doi.org/10.1126/science.1061051

[94] G. Hitoki, T. Takata, J. Kondo, M. Hara, H. Kobayashi, K. Domen, An oxynitride, TaON, as an efficient water oxidation photocatalyst under visible light, Chem. Commun. 21(16) (2002) 1698-99. https://doi.org/10.1039/B202393H

[95] K. Maeda, K. Teramura D. Lu, T. Takata, N. Saito, Y. Inoue, K. Domen, Photocatalyst releasing hydrogen from water, Nature 440 (2006) 295-305. https://doi.org/10.1038/440295a

[96] K. Vijayasankara, N.Y. Hebalkara, H.G. Kimb, P.H. Borse, Controlled band energetics in Pb-Fe-Nb-O metal oxide composite system to fabricate efficient visible light photocatalyst, J. Ceram. Process. Res. 14(4) (2013) 557-562.

[97] M. Cherevatskaya, M. Neumann, S. Füldner, C. Harlander, S. Kümmel, S. Dankesreiter, A. Pfitzner, K. Zeitler, B. König, Visible-light-promoted stereoselective alkylation by combining heterogeneous photocatalysis with organocatalysis, Angew. Chem. Int. Ed. 51(17) (2012) 4062-4066. https://doi.org/10.1002/anie.201108721

[98] Thibert, F. A. Frame, E. Busby, D.S. Larsen, Primary photodynamics of water-solubilized two-dimensional CdSe nanoribbons, J. Phys. Chem. C 115(40) (2011) 19647-19658. https://doi.org/10.1021/jp206828y

[99] Y.-H. Liu, V.L. Wayman, P.C. Gibbons, R.A. Loomis, W.E. Buhro, Origin of high photoluminescence efficiencies in CdSe quantum belts, Nano Lett. 10(1) (2009) 352-357.

[100] T. Kako, Z. Zou, J. Ye, Photocatalytic oxidation of 2-propanol in the gas phase over cesium bismuth niobates under visible light irradiation, Res. Chem. Intermed. 31 (2005) 359–364. https://doi.org/10.1163/1568567053956563

[101] H.G. Kim, D.W. Hwang, J.S. Lee, An undoped, single-phase oxide photocatalyst working under visible light, J. Am. Chem. Soc. 126 (2004) 8912–8913. https://doi.org/10.1021/ja049676a

[102] T. Kako, J. Ye, Photocatalytic decomposition of acetaldehyde over rubidium bismuth niobates under visible light irradiation, Mater. Trans. 46 (2005) 2699–2703. https://doi.org/10.2320/matertrans.46.2694

[103] Muktha, M.H. Priya, G. Madras, T.N. Guru Row, Synthesis, structure, and photocatalysis in a new structural variant of the aurivillius phase: $LiBi_4M_3O_{14}$ (M = Nb, Ta), J. Phys. Chem. B 109 (2005) 11442–11449. https://doi.org/10.1021/jp051228h

[104] L.M. Torres-Martínez, I. Juárez-Ramírez, J.S. Ramos-Garza, F. Vázquez-Acosta, S.W. Lee, Sol-gel preparation of Bi_2InTaO_7 and its photocatalytic behavior for organic compounds degradation, Mater. Sci. Forum 658 (2010) 491–494. https://doi.org/10.4028/www.scientific.net/MSF.658.491

[105] X. Li, S. Ouyang, N. Kikugawa, J. Ye, Novel Ag_2ZnGeO_4 photocatalyst for dye degradation under visible light irradiation, Appl. Catal. A: Gen. 334 (2008) 51–58. https://doi.org/10.1016/j.apcata.2007.09.033

[106] Z. Shan, W. Wang, X. Lin, H. Ding, F. Huang, Photocatalytic degradation of organic dyes on visible-light responsive photocatalyst $PbBiO_2Br$, J. Solid State Chem. 181 (2008) 1361–1366. https://doi.org/10.1016/j.jssc.2008.03.001

[107] F. Mei, C. Liu, Effect of annealing temperature on binary TiO_2:SiO_2 nanocrystalline thin films, J. Korean Phys. Soc. 48(6) (2006) 1509-1513.

[108] K.Y. Jung, S.B. Park, Photoactivity of SiO_2/TiO_2 and ZrO_2/TiO_2 mixed oxides prepared by sol-gel method, Mater. Lett. 58(22-23) (2004) 2897-2900. https://doi.org/10.1016/j.matlet.2004.05.015

[109] A.M. Soylu, M. Polat, D.A. Erdogan, Z. Say, C. Yıldırım, Ö. Birer, E. Ozensoy, TiO_2–Al_2O_3 binary mixed oxide surfaces for photocatalytic NO_x abatement, Appl. Surf. Sci. 318 (2014) 142–149. https://doi.org/10.1016/j.apsusc.2014.02.065

[110] S.M. Andonova, G.S. Senturk, E. Kayhan, E. Ozensoy, Nature of the Ti–Ba interactions on the $BaO/TiO_2/Al_2O_3$ NO_x storage system, J. Phys. Chem. C 113 (2009) 11014–11026. https://doi.org/10.1021/jp9005026

[111] S.M. Andonova, G.S. Senturk, E. Ozensoy, Fine-tuning the dispersion and the mobility of BaO domains on NO_x storage materials via TiO_2 anchoring sites, J. Phys. Chem. C 114 (2010) 17003–17016. https://doi.org/10.1021/jp102555c

[112] D.A.H. Hanaor, C.C. Sorrell, Review of the anatase to rutile phase transformation, J. Mater. Sci. 46 (2011) 855–874. https://doi.org/10.1007/s10853-010-5113-0

[113] Bajorowicz, A. Cybula, M. J. Winiarski, T. Klimczuk, A. Zaleska, Surface properties and Photocatalytic activity of $KTaO_3$, CdS, MoS_2 semiconductors and their binary and ternary semiconductor composites, Molecules 19 (2014)15339-15360. https://doi.org/10.3390/molecules190915339

[114] S. Zhong, L. Zhang, Z. Huang, S. Wang, Mixed-solvothermal synthesis of CdS micro/nanostructures and their optical properties, Appl. Surf. Sci. 257 (2011) 2599–2603. https://doi.org/10.1016/j.apsusc.2010.10.029

[115] Y. Liu, H. Yu, X. Quan, S. Chen, Green synthesis of feather-shaped MoS_2/CdS photocatalyst for effective hydrogen production, Int. J. Photoenergy 2013, 2013, 247516–24752.

[116] Y. Lin, Z. Geng, H. Cai, L. Ma, J. Chen, J. Zeng, N. Pan, X. Wang, Ternary graphene–TiO_2–Fe_3O_4 nanocomposite as a recollectable photocatalyst with enhanced durability, Eur. J. Inorg. Chem. (2012) 4439–4444. https://doi.org/10.1002/ejic.201200454

[117] L. Zhang, Y. Zhu, A review of controllable synthesis and enhancement of performances of bismuth tungstate visible-light-driven photocatalysts, Catal. Sci. Technol. 2 (2012) 694–706. https://doi.org/10.1039/c2cy00411a

[118] Zhang,Y. F. Zhu, Synthesis of square Bi_2WO_6 nanoplates as high-activity visible-light-driven photocatalysts, Chem. Mater. 17(13) (2005) 3537-3545. https://doi.org/10.1021/cm0501517

[119] H.B. Fu, L.W. Zhang, W.Q. Yao, Y.F. Zhu, Photocatalytic properties of nanosized Bi_2WO_6 catalysts synthesized via a hydrothermal process, Appl. Catal. B 66 (2006) 100-110. https://doi.org/10.1016/j.apcatb.2006.02.022

[120] L. Zhang, W. Wang, Z. Chen, L. Zhou, H. Xu, W. Zhu, Fabrication of flower-like Bi_2WO_6 superstructures as high performance visible-light driven photocatalysts, J. Mater. Chem. 17 (2007) 2526-2532. https://doi.org/10.1039/b616460a

[121] L. Zhang, H. Wang, Z. Chen, P.K. Wong, J. Liu, Bi_2WO_6 micro/nano-structures: Synthesis, modifications and visible-light-driven photocatalytic applications, Appl. Catal., B 106(1-2) (2011) 1-13. https://doi.org/10.1016/j.apcatb.2011.05.008

[122] L. Zhang, W.Z. Wang, L. Zhou, H.L. Xu, Bi_2WO_6 nano-and microstructures: shape control and associated visible-light-driven photocatalytic activities, Small 23(9) (2007) 1618-1624. https://doi.org/10.1002/smll.200700043

[123] K. Vijayasankar, N.Y. Hebalkar, H.G. Kim, P.H. Borse, Controlled band energetics in Pb-Fe-Nb-O metal oxide composite system to fabricate efficient visible light photocatalyst, J. Ceram. Process. Res. 14(4) (2013) 557-562.

[124] S.P. Singh, A.K. Singh, D. Pandeya, H. Sharma, and Om Parkash, Crystallographic phases, phase transitions and barrier layer formation in $(1-x)[Pb(Fe_{1/2}Nb_{1/2})O_3]$-$xPbTiO_3$, J. Mater. Res. 18 (2003) 2677-2687. https://doi.org/10.1557/JMR.2003.0374

[125] R. Sun, W. Tan, B. Fang, Perovskite phase formation and electrical properties of $Pb(Fe_{1/2}Nb_{1/2})O_3$ ferroelectric ceramicse, Phys. Status Solidi A. 206(2) (2009) 326-331. https://doi.org/10.1002/pssa.200824432

[126] R.R. Schaller, Technological innovation in the semiconductor industry: a case study of the international technology roadmap for semiconductors (ITRS), George Mason University (2004).

[127] G.D. Wilk, R.M. Wallace, J.M. Anthony, High-κ gate dielectrics: current status and materials properties considerations, J. Appl. Phys. 89 (2001) 5243-5249. https://doi.org/10.1063/1.1361065

[128] F.B. Ergin, R. Turan, S.T. Shishiyanu, Effect of γ-radiation on HfO_2 based MOS capacitor, Nucl. Inst. Meth. Phys. Res. B: Beam Interactions with Materials and Atoms 268 (2010) 1482-1485.

[129] M.A. Khaskheli, P. Wu, A.M. Soomro, M. Khan, M.E. Asadullah, M.S. Kalhoro, Fabrication and electrical characteristic of quaternary ultrathin HfTiErO thin films for MOS devices grown by RF sputtering**,** Chem. Mater. Res. 3(4) (2013) 41-47.

[130] Q. Tao, A. Kueltzo, M. Singh, Atomic layer deposition of HfO_2, TiO_2, and $Hf_xTi_{1-x}O_2$ using metal (diethylamino) precursors and HfO_2, J. Electrochem. Soc. 158 (2008) G27-G33. https://doi.org/10.1149/1.3522758

[131] D.Y. Cho, S.J. Oh, Y. Chang Y, Role of oxygen vacancy in $HfO_2/SiO_2/Si$ (100) interfaces. Appl. Phys. Lett. 88 (2006) 193502-193503. https://doi.org/10.1063/1.2201050

[132] F.Y. Xiao, J. Xing, L. Wu, Z.P. Chen, X.L. Wang, H.G. Yang, Assembly ultrathin $PbBiO_2Br$ nanosheets with enhanced visible light Photocatalytic property, R. Soc. Chem. (2013).

[133] Z. Deng, D. Chen, B. Peng, F. Tang, From bulk metal Bi to two-dimensional well-crystallized BiOX (X = Cl, Br) micro-and nanostructures: Synthesis and characterization, Cryst. Growth Des. 8(8) (2008) 2995-3003. https://doi.org/10.1021/cg800116m

[134] F.Y. Xiao, J. Xing, L. Wu, Z.P. Chen, X.L. Wanga, H. G. Yang, Assembly ultrathin $PbBiO_2Br$ nanosheets with enhanced visible light photocatalytic property, RSC Adv. 3(27) (2013) 10687-10690. https://doi.org/10.1039/c3ra41324a

[135] L. Cademartiri, G.A. Ozin, Ultrathin nanowires—A materials chemistry perspective, Adv. Mater. 21(9) (2009) 1013-1020. https://doi.org/10.1002/adma.200801836

[136] K. Richardson, W. Steffen, H.J. Schellnhuber, J. Alcamo, T. Barker, D.M. Kammen, R. Leemans, D. Liverman, M. Munasinghe, B. Osman-Elsha, N. Stern, O. Waever, Synthesis report from climate change: global risks, Challenges & Decisions, University of Copenhagen (2009).

[137] G.A. Olah, A. Goeppert, G.K.S. Prakash, Beyond oil and gas: The methanol economy, Wiley-VCH, Weinheim (2006) 212.

[138] K. Oppelt, D.A.M. Egbe, U. Monkowius, M. List, M. Zabel, N.S. Sariciftci, G. Knör, Luminescence and spectroscopic studies of organometallic rhodium and rhenium multichromophore systems carrying polypyridyl acceptor sites and

phenylethynyl antenna subunits, J. Organomet. Chem. 696 (2011) 2252-2258. https://doi.org/10.1016/j.jorganchem.2010.11.008

[139] Portenkirchner, K. Oppelt, C. Ulbricht, A.M. Egbe , H. Neugebauer, G. Knör, N. S. Sariciftci, Electrocatalytic and photocatalytic reduction of carbon dioxide to carbon monoxide using the alkynyl-substituted rhenium(I) complex (5,50-bisphenylethynyl-2,20-bipyridyl)Re(CO)$_3$Cl, J. Organomet. Chem. 716 (2012) 19-25.

[140] J. Hawecker, J.M. Lehn, R. Ziessel, H. Chim, Photochemical and electrochemical reduction of carbon dioxide to carbon monoxide mediated by (2, 2′-Bipyridine) tricarbonylchlororhenium(I) and related complexes as homogeneous catalysts, Acta 69(8) (1986) 1990-2012. https://doi.org/10.1002/hlca.19860690824

[141] K. Koike, H. Hori, M. Ishizka, J.R. Westwell, K. Takeuchi, T. Ibusuki, K. Enjouji, H. Konno, K. Sakamoto, O. Ishitani, Key process of the photocatalytic reduction of CO_2 using [Re(4,4‘-X_2-bipyridine)(CO)$_3$$PR_3$]$^+$ (X = CH_3, H, CF_3; PR_3 = phosphorus ligands): dark reaction of the one-electron-reduced complexes with CO_2, Organomet. 16(26) (1997) 5724-5729. https://doi.org/10.1021/om970608p

[142] Fujishima, Electrochemical photolysis of water at a semiconductor electrode, Nature 238 (1971) 37–38. https://doi.org/10.1038/238037a0

[143] Del Valle, F. Del Valle, J.A. Villoria De La Mano, M. C. Álvarez-Galván, J.L. G. Fierro, Photocatalytic water splitting under visible light: concept and materials requirements, Adv. Chem. Eng. 36 (2009) 111–143.

[144] Kato, K. Asakura, A. Kudo, Highly efficient water splitting into H_2 and O_2 over lanthanum-doped NaTaO photocatalysts with high crystallinity and surface nanostructure, J. Am. Chem. Soc. 125 (2003) 3082-3092. https://doi.org/10.1021/ja027751g

[145] D. Yokoyama, H. Hashiguchi, K. Maeda, T. Minegishi, T. Takata, R. Abe, J. Kubota, K. Domen, Ta_3N_5 photoanodes for water splitting prepared by sputtering, Thin Solid Films 519(7) (2011) 2087–2092. https://doi.org/10.1016/j.tsf.2010.10.055

[146] K. Maeda, T. Takata, M. Hara, N. Saito, Y. Inoue, H. Kobayashi, K. Domen, GaN: ZnO solid solution as a photocatalyst for visible-light-driven overall water splitting, J. Am. Chem. Soc. 127 (2005) 8286-8287. https://doi.org/10.1021/ja0518777

[147] K. Maeda, K. Domen, New non-oxide photocatalysts designed for overall water splitting under visible light, J. Phys. Chem. C 111(22) (2007) 7851-7861.

[148] T. Mishima, M. Matsuda, M. Miyake, Visible-light photocatalytic properties and electronic structure of Zr-based oxynitride, Zr_2ON_2, derived from nitridation of ZrO_2, Appl. Catal. A: Gen. 324(1-2) (2007) 77–82. https://doi.org/10.1016/j.apcata.2007.03.017

[149] M.M. Hassan, H. Dylla, L.N. Mohammad, T. Rupnow, Effect of application methods on the effectiveness of titanium dioxide as a photocatalyst compound to concrete pavement, Presented at 89th Annual Meeting of the Transportation Research Board, Washington, D.C. (2010).

[150] J. Yang, G. Jiang, G, Experimental study on properties or pervious concrete pavement materials. Cem. Concr. Res. 33 (2003) 381-386. https://doi.org/10.1016/S0008-8846(02)00966-3

[151] M. Miyauchi, A. Nakajima, T. Watanabe, K. Hashimoto, Photocatalysis and photoinduced hydrophilicity of various metal oxide thin films, Chem. Mater. 14 (2002) 2812–2816. https://doi.org/10.1021/cm020076p

[152] S. Navarro, J. Fenoll, N. Vela, E. Ruiz, G. Navarro, Photocatalytic degradation of eight pesticides in leaching water by use of ZnO under natural sunlight, J. Hazard. Mater. 172 (2009) 1303–1310. https://doi.org/10.1016/j.jhazmat.2009.07.137

[153] A.A. Abdel, S.A. Mahmoud, A.K. Aboul-Gheit, Sol-gel and thermally evaporated nanostructured thin ZnO films for photocatalytic degradation of trichlorophenol, Nanoscale Res. Lett. 4 (2009) 627–634. https://doi.org/10.1007/s11671-009-9290-1

[154] C.C. Chen, Degradation pathways of ethyl violet by photocatalytic reaction with ZnO dispersions, J. Mol. Catal. A: Chem. 264 (2006) 82–92. https://doi.org/10.1016/j.molcata.2006.09.013

[155] Xu, W. Wang, W. Zhu, Shape evolution and size-controllable synthesis of Cu_2O octahedra and their morphology-dependent photocatalytic properties, J. Phys. Chem. B 110 (2006) 13829–13834. https://doi.org/10.1021/jp061934y

[156] J.-Y Ho, M.H. Huang, Synthesis of submicrometer-sized Cu_2O crystals with morphological evolution from cubic to hexapod structures and their comparative photocatalytic activity, J. Phys. Chem. C 113 (2009) 14159–14164. https://doi.org/10.1021/jp903928p

[157] L. Huang, F. Peng, H. Yu, H. Wang, Preparation of cuprous oxides with different sizes and their behaviours of adsorption, visible-light driven photocatalysis and photocorrosion, Solid State Sci. 11 (2009) 129–138. https://doi.org/10.1016/j.solidstatesciences.2008.04.013

[158] Watcharenwong, W. Chanmanee, N.R. de Tacconi, C.R. Chenthamarakshan, P. Kajitvichyanukul, K. Rajeshwar, Anodic growth of nanoporous WO_3 films: morphology, photoelectrochemical response and photocatalytic activity for methylene blue and hexavalent chrome conversion, J. Electroanal. Chem. 612 (2008) 112–120. https://doi.org/10.1016/j.jelechem.2007.09.030

[159] Luo, M. Hepel, Photoelectrochemical degradation of naphthol blue black diazo dye on WO_3 film electrode, Electrochim. Acta 46 (2001) 2913–2922. https://doi.org/10.1016/S0013-4686(01)00503-5

[160] Y. Bessekhouad, D. Robert, J.-V. Weber, Photocatalytic activity of Cu_2O/TiO_2, Bi_2O_3/TiO_2 and $ZnMn_2O_4/TiO_2$ heterojunctions, Catal. Today 101 (2005) 315–321. https://doi.org/10.1016/j.cattod.2005.03.038

[161] Z. Ai, Y. Huang, S. Lee, L. Zhang, Monoclinic α-Bi_2O_3 photocatalyst for efficient removal of gaseous NO and HCHO under visible light irradiation, J. Alloys Compd. 509 (2011) 2044–2049. https://doi.org/10.1016/j.jallcom.2010.10.132

[162] S. Kohtani, J. Hiro, N. Yamamoto, A. Kudo, K. Tokumura, R. Nakagaki, Adsorptive and photocatalytic properties of Ag-loaded $BiVO_4$ on the degradation of 4-n-alkylphenols under visible light irradiation, Catal. Commun. 6 (2005) 185-195. https://doi.org/10.1016/j.catcom.2004.12.006

[163] X. Hu, C. Hu, Preparation and visible-light photocatalytic activity of Ag_3VO_4 powders, J. Solid State Chem. 180 (2007) 725–732. https://doi.org/10.1016/j.jssc.2006.11.032

[164] D. Ye, D. Li, W. Zhang, M. Sun, Y. Hu, Y. Zhang, X. Fu, A new photocatalyst $CdWO_4$ prepared with a hydrothermal method, J. Phys. Chem. C 112 (2008) 17351–17356. https://doi.org/10.1021/jp8059213

[165] T. Yan, L. Li, W. Tong, J. Zheng, Y. Wang, G. Li, $CdWO_4$ polymorphs: Selective preparation, electronic structures, and photocatalytic activities, J. Solid State Chem. 184 (2011) 357–364. https://doi.org/10.1016/j.jssc.2010.12.013

[166] X. Lin, T. Huang, F. Huang, W. Wang, J. Shi, Photocatalytic activity of a Bi-based oxychloride Bi_4NbO_8Cl, J. Mater. Chem. 17 (2007) 2145–2150. https://doi.org/10.1039/b615903f